Computer Methods in Biomechanics and Biomedical Engineering, Vol. 4, pp. 93–126
Reprints available directly from the publisher
Photocopying permitted by license only

Musculoskeletal Model of the Upper Limb Based on the Visible Human Male Dataset

BRIAN A. GARNER and MARCUS G. PANDY*

Department of Mechanical Engineering and Department of Kinesiology, University of Texas at Austin, Austin, Texas 78712, USA

(Received 4 July 1999; In final form 28 April 2000)

A mathematical model of the human upper limb was developed based on high-resolution medical images of the muscles and bones obtained from the Visible Human Male (VHM) project. Three-dimensional surfaces of the muscles and bones were reconstructed from Computed Tomography (CT) images and Color Cryosection images obtained from the VHM cadaver. Thirteen degrees of freedom were used to describe the orientations of seven bones in the model: clavicle, scapula, humerus, radius, ulna, carpal bones, and hand. All of the major articulations from the shoulder girdle down to the wrist were included in the model. The model was actuated by 42 muscle bundles, which represented the actions of 26 muscle groups in the upper limb. The paths of the muscles were modeled using a new approach called the Obstacle-set Method [33]. The calculated paths of the muscles were verified by comparing the muscle moment arms computed in the model with the results of anatomical studies reported in the literature. *In-vivo* measurements of maximum isometric muscle torques developed at the shoulder, elbow, and wrist were also used to estimate the architectural properties of each musculotendon actuator in the model. The entire musculoskeletal model can be reconstructed using the data given in this paper, along with information presented in a companion paper which defines the kinematic structure of the model [26].

Keywords: Imaging; Musculoskeletal modeling; Muscle paths; Musculotendon properties; Upper limb; Shoulder; Elbow; Wrist

INTRODUCTION

Computer models are playing an increasingly important role in biomechanical studies of movement. This interest is driven by the belief that modeling can provide significant insight into how the neuromuscular and musculoskeletal systems interact to produce movement [1–3]. Much of the modeling work to date has been directed at the lower limb, mainly because of the considerable interest in locomotion [4–8]. Many workers have also developed mathematical models of the upper

*Corresponding author.

limb, although interest here has centered on specific aspects of shoulder-, elbow-, and wrist-joint function. DeLuca [9] and Poppen [10] developed simple two-dimensional models of the glenohumeral joint to calculate the forces acting on the humeral head during elevation of the arm in the scapular plane. Hogfors [11], Karlsson [12], van der Helm [13] and Happee [14] used more elaborate three-dimensional models of the shoulder girdle to study function of the muscles, ligaments, and bones during movement. Models of varying complexity have also been used to describe and explain the moment- and force-generating capacities of the muscles crossing the elbow [15–18] and the wrist [18–21].

A complete musculoskeletal model of the upper limb is presently not available in the literature. Seireg [22] developed a model that includes all the major joints from the shoulder girdle down to the wrist, except for the articulation between the scapula and the thorax. Their model also neglects the carrying angle of the elbow, and assumes that the path of each muscle may be modeled as a straight line joining the origin and insertion sites of the actuator. The models described by Raikova [23] and Pigeon [24] are even more simplified. Pigeon [24] developed a planar model of the upper limb, with the shoulder, elbow, and wrist represented as simple hinge joints. Raikova [23] developed a three-dimensional model of the upper limb, but this model does not take into account the movements of the clavicle and scapula. Simple models are appealing from the standpoint that they involve fewer variables, which simplifies analysis and interpretation of the results; however, simple models of the upper limb will find limited application in studies of unrestrained reaching and throwing, because these movements involve the coordinated motion of all the joints [25].

We have developed a musculoskeletal model of the upper limb that includes all the major joints from the shoulder girdle down to the wrist; not considered in the model are the separate joints and muscles of the hand. The model is based on high-resolution medical images of the muscles and bones obtained from the Visible Human Male (VHM) project. Thirteen degrees of freedom were used to describe the relative positions and orientations of seven bones: clavicle, scapula, humerus, radius, ulna, carpal bones, and hand. The kinematic structure of the model has been described previously by Garner [26]. The main aim of this paper is to present a model of the musculoskeletal geometry (*i.e.*, musculotendon paths) as well as estimates of the architectural properties (*i.e.*, muscle volume, physiological cross-sectional area, fiber length, pennation angle, and tendon rest length) for each of the major muscles crossing the shoulder, elbow, and wrist. Measurements of muscle moment arms and muscle architecture reported in the literature are used to evaluate the geometry and properties of the muscles assumed in the model.

METHODS

Bone and Muscle Reconstructions

The VHM dataset represents a three-dimensional "snapshot" of an intact human body, and is essentially a digital cadaver. Surface boundaries of the bones and muscles from the right side of the body were identified using a color-thresholding formula, and were reconstructed using the Marching Cubes Algorithm reported by Lorensen [27]. Bones of the thorax (sternum, ribs, and vertebrae), clavicle, scapula, carpal bones, and hand were reconstructed from Computed Tomography (CT) images with a resolution of about 1.7 mm. Bones of the humerus, ulna, and radius, because they fell outside the frame of the CT images, were reconstructed from reduced versions of the VHM color cryosection images with a resolution of about 1.3 mm. The muscles were reconstructed from a reduced set of the VHM color cryosection images with a resolution of about 4 mm.

The surfaces of the bones and muscles were reconstructed in the form of very dense triangle meshes. A geometry-preserving decimation

algorithm [28] was then applied to each reconstructed surface in order to reduce its mesh density by about 90%. A computer-generated rendering of the reconstructed bones and muscles is shown in Figure 1.

Joint Models

Thirteen degrees of freedom described the relative positions and orientations of the clavicle, scapula, humerus, ulna, radius, carpal bones, and hand in the model. The articulation between the scapula and the thorax was modeled using two holonomic constraints (see Garner [26] for details). The joints of the shoulder girdle – the sternoclavicular joint, the acromioclavicular joint, and the glenohumeral joint – were each modeled as a 3 degree-of-freedom ball-and-socket joint. The articulations at the elbow and wrist – humeroulnar flexion-extension, radioulnar pronation-supination, radiocarpal flexion-extension, and radiocarpal radial-ulnar deviation – were each modeled as a 1 degree-of-freedom hinge joint. The positions of the joint centers and the positions and orientations of the joint axes of rotation were calculated using the three-dimensional surfaces of the reconstructed bones. Details of the kinematic structure assumed for the VHM upper-limb model are given in Garner [26].

Muscle-path Model

Many of the muscles that span the shoulder are fan-shaped and attach over large areas of the bones (*e.g.*, trapezius and pectoralis major). Previous workers have modeled the actions of broad muscles by dividing the whole muscle belly into two or more bundles and assigning a separate line of action to each bundle [22, 29–32]. We divided each muscle belly into separate bundles according to groupings of muscle fascicles reported by Johnson [32]. Based on the results of van der Helm [31], up to four bundles were used to represent the action of each muscle in the model. Muscle attachment sites were found by computing the centroids of the sets of triangles that defined the attachment sites of the muscles on the reconstructed surfaces of the bones. Figure 2 shows how the lines of actions of the trapezius and deltoid were represented in the model.

Forty-two muscle bundles were used to represent the lines of action of 26 muscle groups in the upper limb (Fig. 3). The path of each muscle bundle was calculated using the Obstacle-set method [33]. This method is based on two assumptions: (1) that the centroidal path of each muscle can be idealized as a frictionless elastic band which moves over anatomical constraints provided by the bones and other muscles; and (2) that any anatomical constraint can be modeled as a regular-shaped rigid body or obstacle such as a sphere or a cylinder. Given the locations of the attachment sites of a muscle bundle, the positions of any fixed *via* points along the muscle path, and the size and position and orientation of each obstacle, the path of the muscle can be calculated for the entire range of motion of each joint spanned by the muscle. The locations of the fixed *via* points and the size and position and orientation of each obstacle were chosen so that the path of each modeled muscle matched the locus of cross-sectional centroids of the reconstructed muscle obtained from the VHM dataset. Parameters defining the paths of all the muscles in the model are given in the Appendix. Figures 4–7 show computer-generated renderings of the paths calculated for some of the muscles. Figure 8 specifies the bones to which each muscle is attached as well as the various joints crossed by each muscle in the model.

Isometric Joint Torque Measurements

Experiments were conducted on three healthy male subjects (age 25 ± 3 years, mass 84 ± 7 kg, and height 185 ± 3 cm). A Biodex dynamometer was used to measure the active torques developed at the shoulder, elbow, and wrist during maximum voluntary isometric contractions of the muscles. At the shoulder, maximum torques were measured in all three planes of movement: flexion-extension,

FIGURE 1 Computer-generated rendering of the bone and muscle surfaces reconstructed from the VHM image dataset. The data representing each surface is in the form of a dense mesh of connected triangles. The triangular meshes shown in the figure have been passed through a geometry-preserving decimation algorithm to reduce the mesh density by about 90% (see text). The reconstructed surface data constitute an accurate, high-resolution, anatomical database from which the upper-limb model was developed (See Colour Plate at back of issue.).

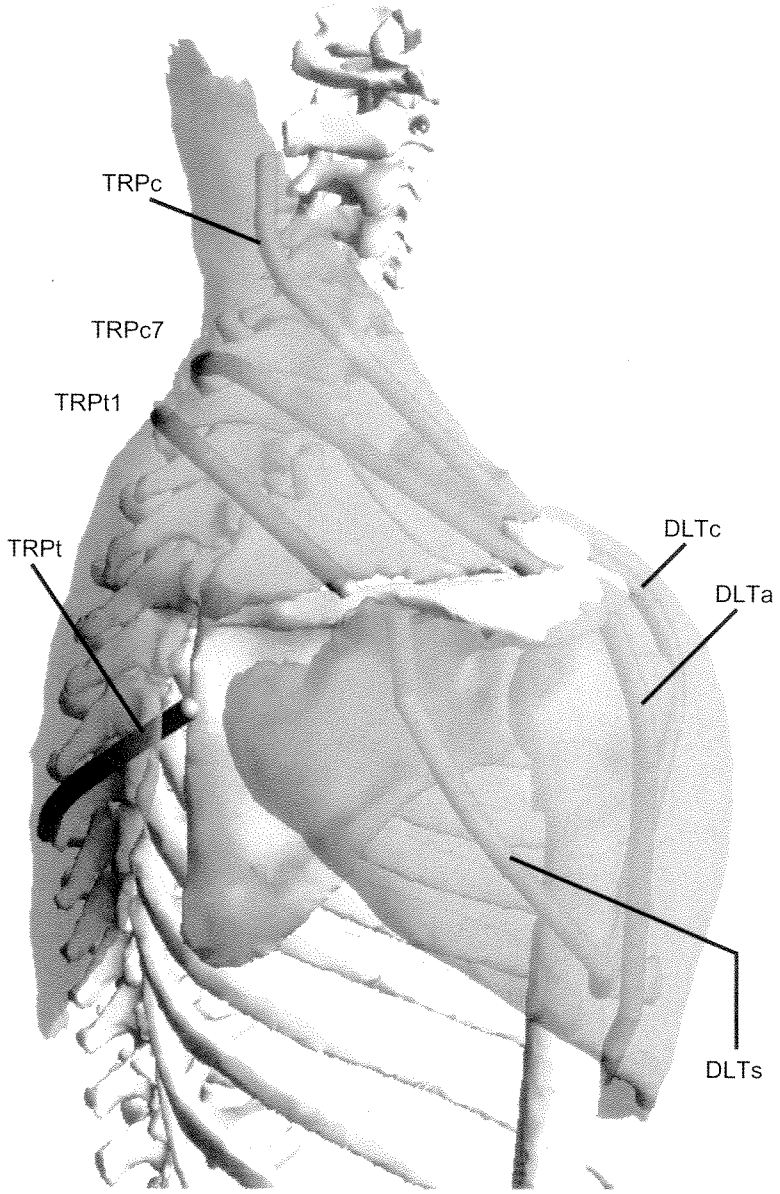

FIGURE 2 Computer-generated rendering of the fan-shaped trapezius and deltoid muscles. Multiple paths were used to model the action of each muscle group. Trapezius was separated into four bundles and deltoid was separated into three bundles in the model (see text for details). Muscle abbreviations are given in Figure 8 and Table I (See Colour Plate at back of issue.).

abduction-adduction, and internal-external rotation. At the elbow, maximum torques were recorded for flexion-extension and pronation-supination. At the wrist, maximum torques were recorded for flexion-extension and radial-ulnar deviation. Measurements were taken over practically the full range of movement of each joint. For example, maximum elbow flexion torque was measured from full extension to 120° of flexion in 15° increments of the elbow flexion angle, with the humerus positioned alongside the torso, and with the wrist fully extended. For each joint, data

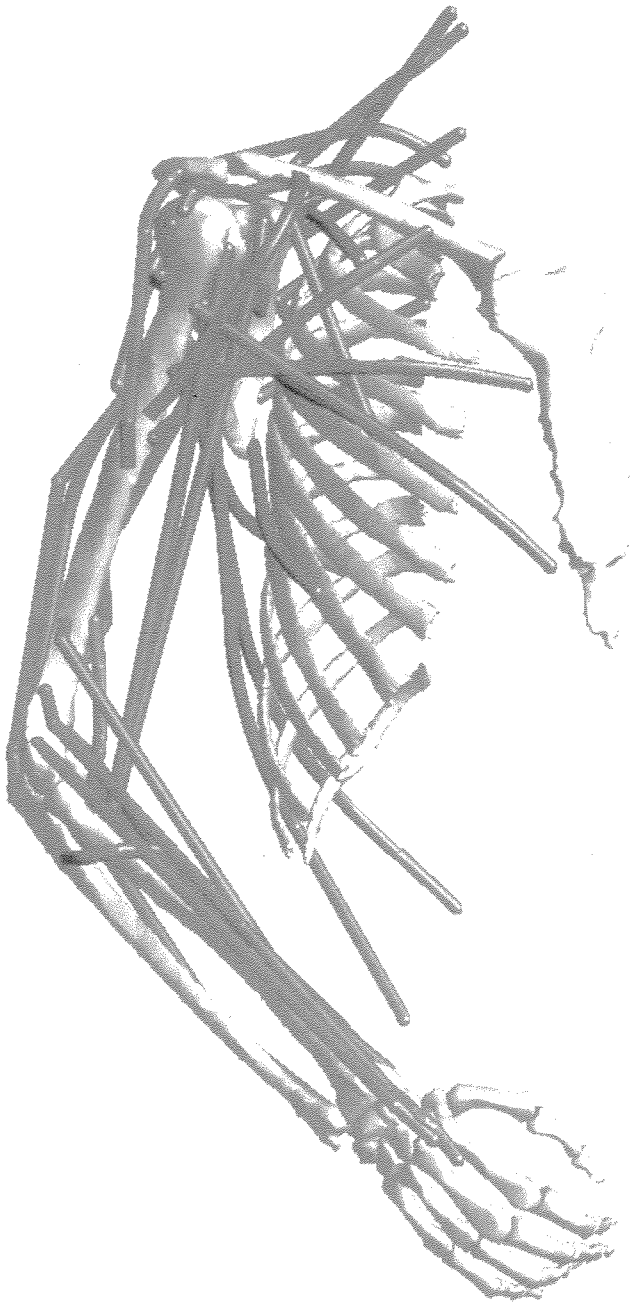

FIGURE 3 Antero-lateral view of the reconstructed bone surfaces overlaid with the modeled muscle paths. Forty-two muscle bundles were used to represent the actions of 26 muscle groups in the upper limb. Muscle abbreviations are given in Figure 8 and Table I (See Colour Plate at back of issue.).

were averaged across the three subjects and then pooled with maximum isometric torque-angle data reported in the literature to create a combined average. A third-order polynomial was then fitted to the combined average torque-angle data obtained for each joint.

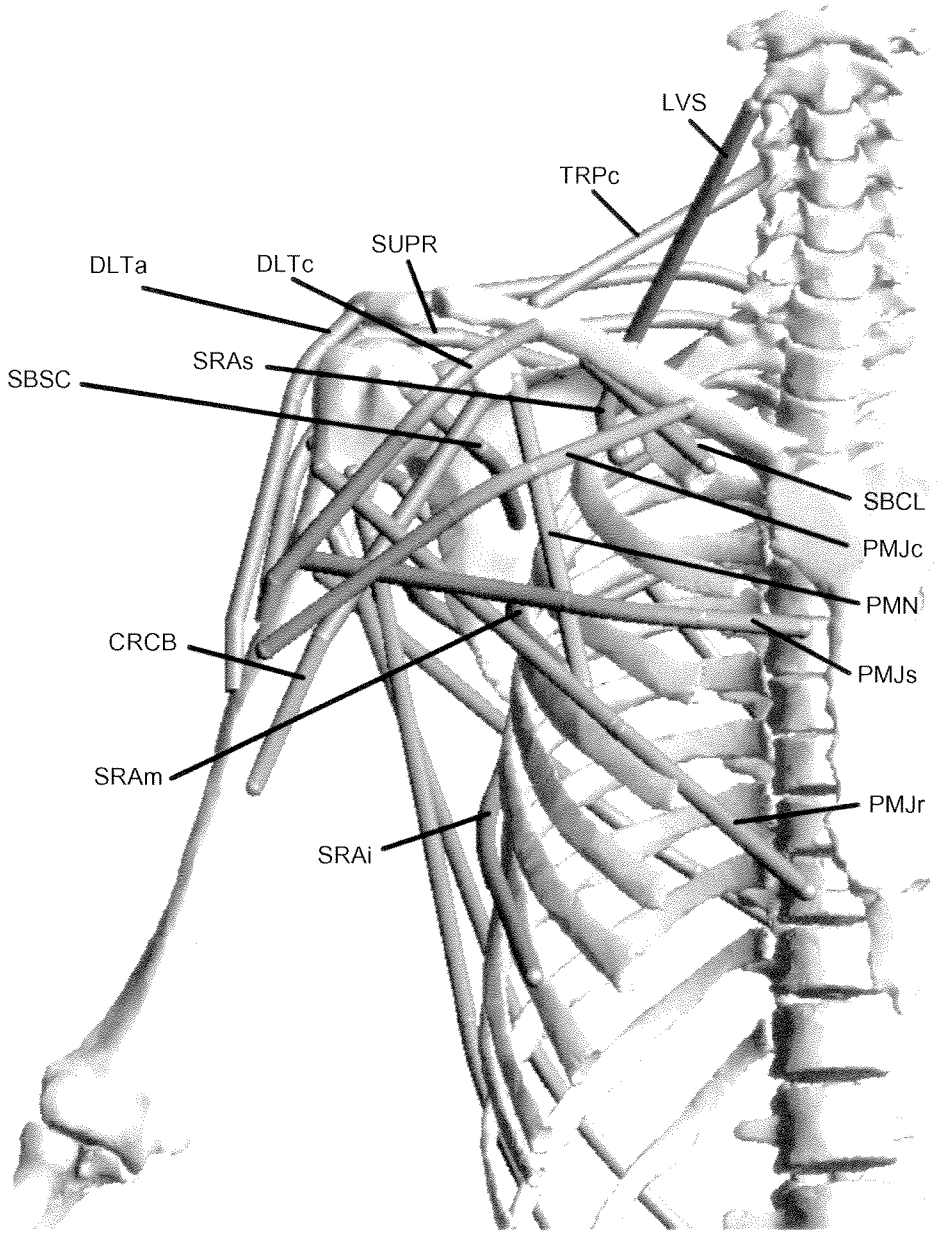

FIGURE 4 Anterior view showing the modeled muscle paths crossing the shoulder. See Figure 8 and Table I for muscle abbreviations (See Colour Plate at back of issue.).

Estimation of Musculotendon Properties

Four parameters are needed to specify the properties of each musculotendon actuator in the model [34]: maximum isometric force (F_o^M) and the corresponding fiber length (L_o^M) and pennation angle (α) of muscle, and tendon slack length (L_s^T). Values of muscle pennation angle were based on experimental data reported in the literature (*e.g.*, Lieber [35] and Winters [36]). For many of the upper-limb muscles, however, and especially for

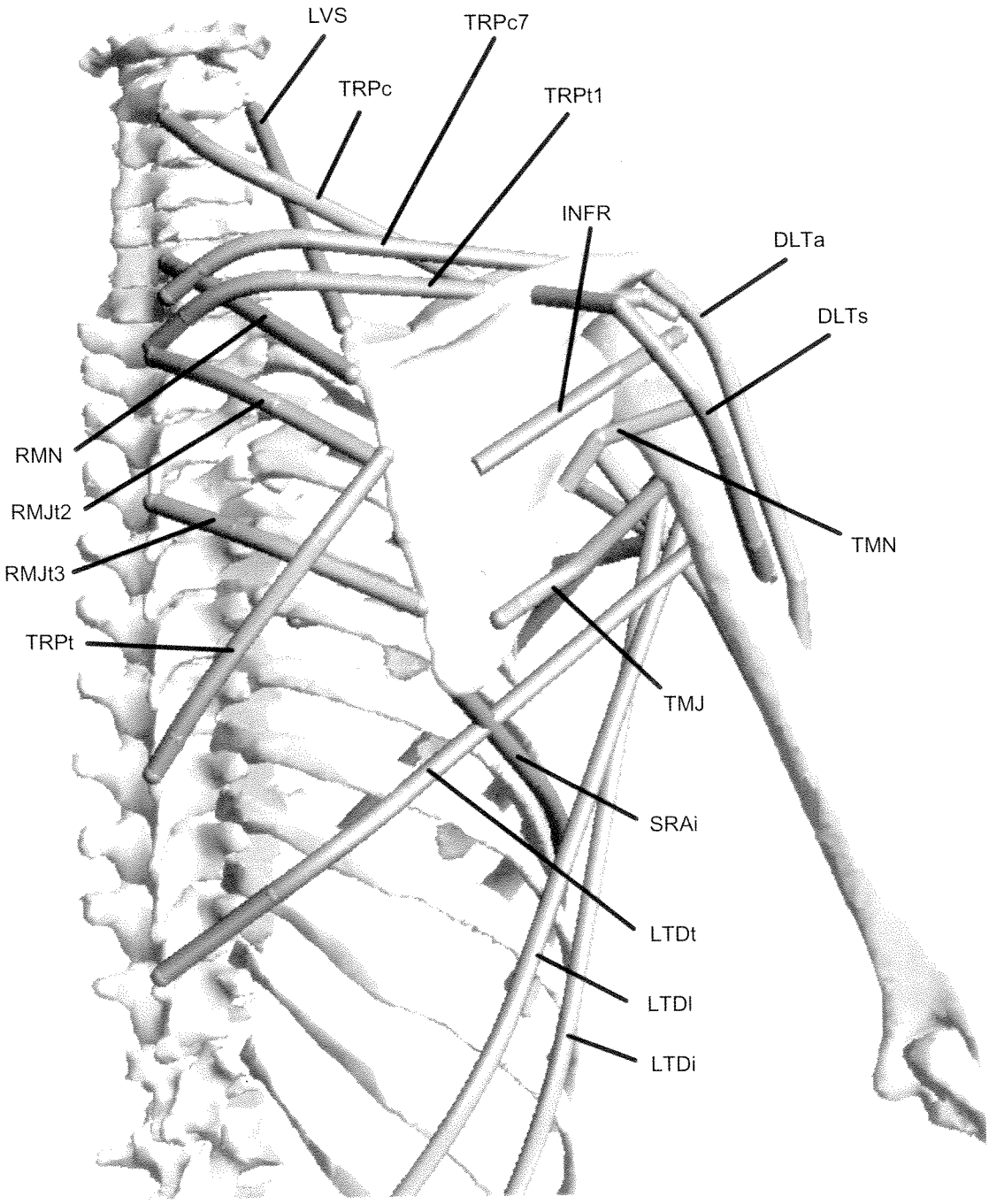

FIGURE 5 Posterior view showing the modeled muscle paths crossing the shoulder. See Figure 8 and Table I for muscle abbreviations (See Colour Plate at back of issue.).

those that cross the shoulder (*e.g.*, serratus anterior, rhomboids, pectoralis major and minor and deltoids), values of pennation angle are not available in the literature. In these cases, muscle pennation angle was assumed to be zero in the model. This assumption is justifiable in view of

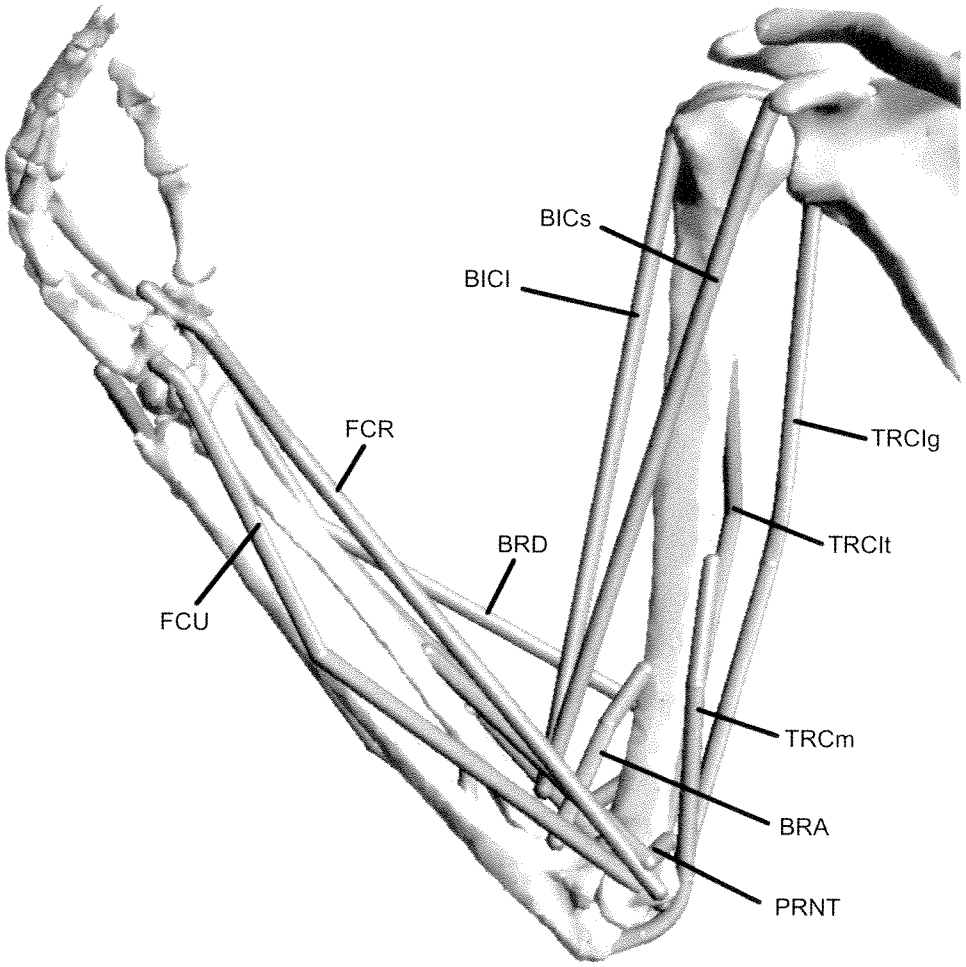

FIGURE 6 Anterior view of the modeled muscle paths crossing the elbow and wrist. Muscle abbreviations are given in Figure 8 and Table I (See Colour Plate at back of issue.).

findings by Amis [37], Winters [36] and Lieber [35] that pennation angles for many of the muscles in the arm and forearm are relatively small (less than 20°).

Muscle volumes were used to constrain the calculated values of F_o^M in the model, whereas maximum and minimum musculotendon lengths were used to constrain estimates of L_o^M and L_s^T. Muscle volumes were found directly from the VHM images by multiplying muscle cross-sectional area by image thickness, and then summing over all the images available for each muscle. Maximum and minimum musculotendon lengths were found using the model assumed for each muscle path. As each joint spanned by the muscle was moved over its full range of motion, the Obstacle-set method [33] was used to find the corresponding maximum and minimum musculotendon lengths of the muscle. (The range-of-motion limits for the model shoulder were based on data reported by Engin [38]. Range-of-motion limits for the model elbow and wrist are indicated in Figs. 10 and 11, respectively.) The constraint equations relating muscle volume to maximum isometric force as well as those relating maximum and minimum musculotendon lengths to muscle-fiber length and tendon slack length are given in Garner [39].

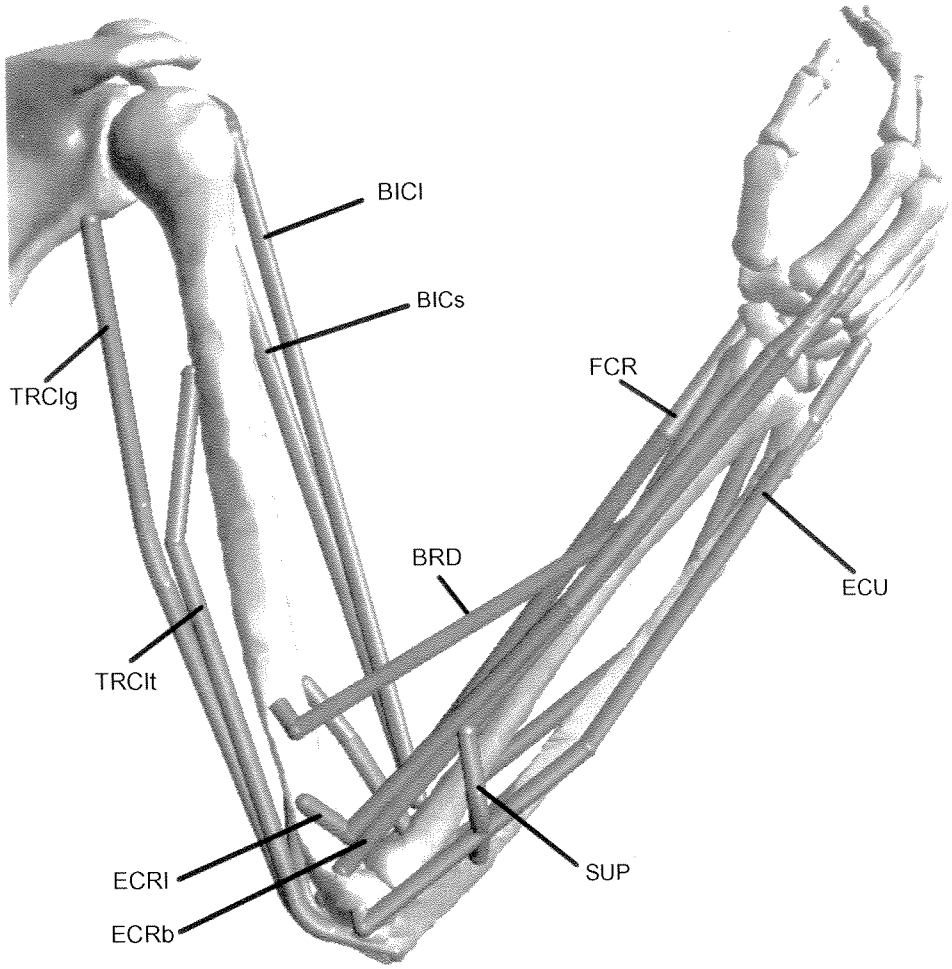

FIGURE 7 Posterior view of the modeled muscle paths crossing the elbow and wrist. See Figure 8 and Table I for muscle abbreviations (See Colour Plate at back of issue.).

Values of F_o^M, L_o^M, and L_s^T for each actuator in the model were found by matching the maximum isometric joint torques in the model to the maximum isometric joint torques measured for human subjects. A two-stage optimization problem was formulated and solved for this purpose. In Stage I, arbitrary values of F_o^M, L_o^M, and L_s^T were assigned to each muscle, and the joint angles and muscle activations for which maximum torque was produced about each joint were calculated. In Stage II, the values of F_o^M, L_o^M, and L_s^T used in Stage I were adjusted until the difference between the computed and measured values of net muscle torque was minimized. The optimization problem was solved iteratively; that is, values of F_o^M, L_o^M, and L_s^T obtained from Stage 2 were used as inputs to Stage 1, and both stages were then repeated until the difference in the calculated and measured values of joint torque was sufficiently small. Details of the optimization procedure used to estimate the properties of each musculotendon actuator in the model are given in [39].

Altogether, 116 different model simulations were performed. For each simulation, the configuration of the upper limb was specified and maximum isometric muscle torque was calculated

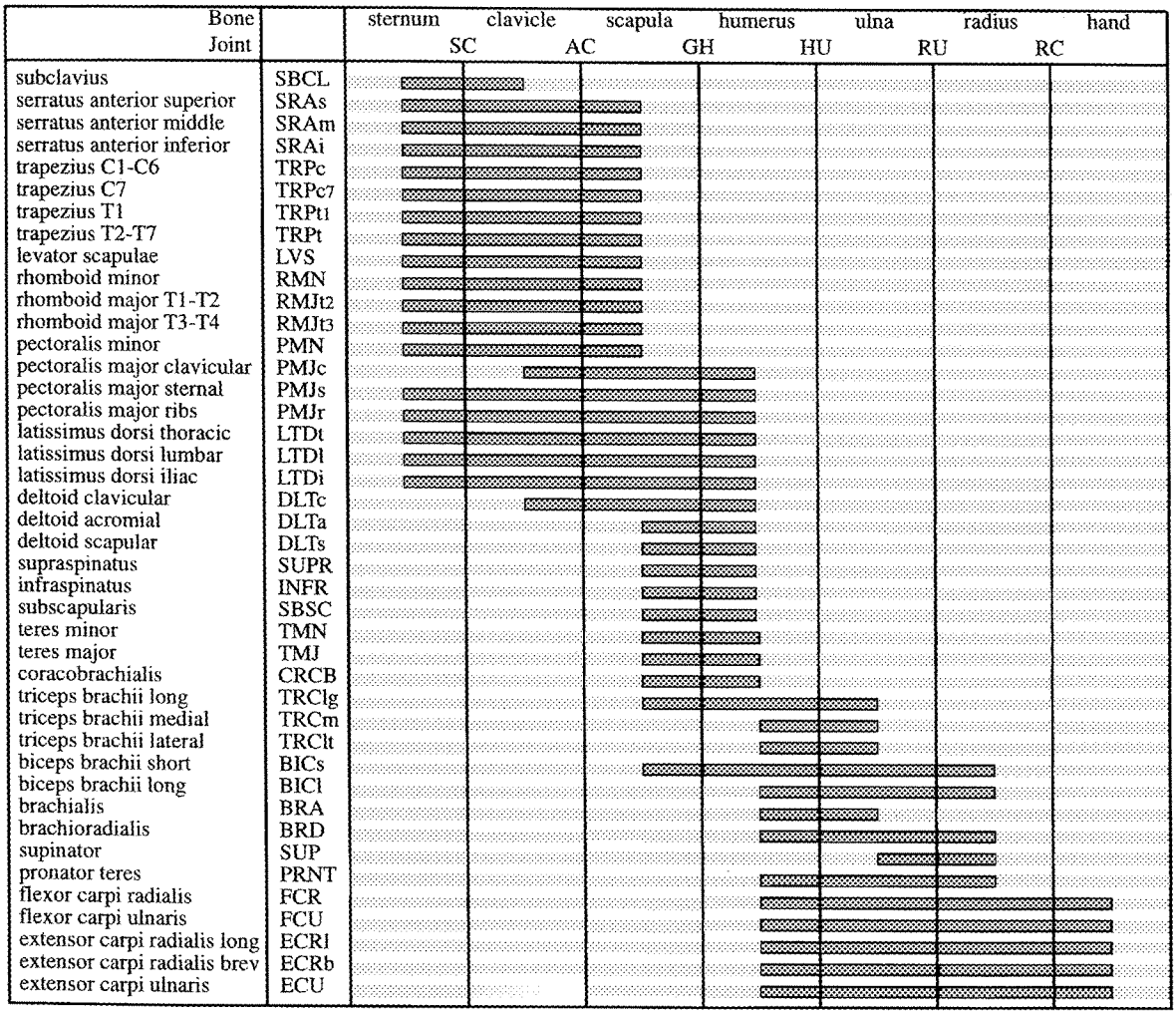

FIGURE 8 Diagram defining the bony attachments and the joints spanned by each muscle in the model. The left edge of each shaded horizontal bar identifies the bone on which the muscle originates, and the right edge of the bar identifies the bone on which the muscle inserts. For example, biceps brachii short head (BICs) originates on the scapula and inserts on the radius; thus, BICs spans the GH, HU, and HU joints. The actual coordinates of the attachment sites for each muscle in the model are defined in Table IV of the Appendix. Most of the muscles in the upper limb span more than one joint and therefore potentially control many degrees of freedom. For example, all portions of latissimus dorsi (LTDt, LTDl, and LTDi) span the SC, AC, and GH joints, which together account for 9 degrees of freedom in the model. Symbols used to represent the various joints included in the upper-limb model are: SC: sternoclavicular joint; AC: acromioclavicular joint; GH: glenohumeral joint; HU: humeroulnar joint; RU: radioulnar joint; RC: radiocarpal joint.

about a given joint; for example, maximum shoulder flexion torque was calculated with the shoulder positioned in 30° flexion, 0° abduction, and 0° internal rotation, and with the elbow flexed to 90°, the forearm in neutral rotation, and the wrist fully extended. Forty-two simulations were performed at the shoulder: 7 simulations each for flexion, extension, abduction, adduction, internal rotation, and external rotation. Forty-six simulations were performed at the elbow: 11 simulations each for flexion and extension and 12 simulations each for forearm pronation and supination.

Finally, twenty-eight simulations were performed at the wrist: 9 simulations each for flexion and extension and 5 simulations each for radial and ulnar deviation.

RESULTS

Muscle volume, maximum and minimum musculotendon lengths, physiological cross-sectional area (PCSA), maximum isometric muscle force, muscle-fiber length, and tendon slack length for each actuator in the model are given in Table I. For all actuators, muscle volume and PCSA are significantly larger than what is reported in the literature. For example, summed PCSA for the deltoids in the model is 82 cm^2 compared to values of around 25 cm^2 reported by Wood [30], Johnson [32] and Bassett [40]. The most likely explanation for differences between the model estimates of muscle PCSA and measured values reported in the literature is that the latter are based on cadaveric specimens obtained from elderly donors, whereas the VHM dataset is based on a relatively young, muscular man (see Fig. 1).

The calculated values of muscle-fiber length are in general agreement with data obtained from anatomical studies. The fiber lengths (average of the separate bundles for each) of deltoid, biceps, triceps, and extensor carpi radialis in the model are respectively 12.80 cm, 14.2 cm, 8.8 cm, and 7.3 cm (Tab. I). Corresponding values reported in the literature are 13.2 cm for deltoid [40], 14.3 cm for biceps [41], 8.3 cm for triceps [41] and 9.9 cm for extensor carpi radialis [20]. Although some differences are apparent between the muscle-fiber lengths calculated for the model and the values reported in the literature, there are also differences in the results obtained from the various anatomical studies. For example, Bassett [40] reported a fiber length of 18 cm for biceps, which is significantly higher than the value of 14 cm given by An [41]. Also, Cutts [42] found fiber lengths of the order of 8 cm for flexor carpi ulnaris, which is roughly twice as long as the lengths reported by Amis [37], Brand [43] and Winters [36].

Very few experimental data are available for tendon slack lengths in the upper limb. Loren [20] measured tendon slack lengths for actuators crossing the wrist, and their results show values of 20.5 cm for extensor carpi radialis brevis, 26.7 cm for extensor carpi radialis longus, and 23.1 cm for flexor carpi radialis. Corresponding values for the model are 26.9 cm, 26.8 cm, and 27.1 cm, respectively (see Tab. I).

Moment Arms

Shoulder

In the model, abduction moment arms of the rotator cuff muscles (anterior, middle, and posterior deltoid, supraspinatus, infraspinatus, and subscapularis) vary continuously with elevation of the humerus in the scapular plane. Liu [44] found that supraspinatus and middle deltoid have the two largest abduction moment arms: the peak value for supraspinatus was 30 mm at 30° abduction and that for middle deltoid was 27 mm at 60° abduction. Peak abduction moment arms for supraspinatus and middle deltoid in the model are 27 mm and 32 mm, respectively (Figs. 9A and B). The anterior bundle of deltoid in the model also has a large abduction moment arm for glenohumeral abduction angles greater than 60° in the scapular plane (not shown in Fig. 9). Although Liu [44] and Otis [45] reported much smaller abduction moment arms for this muscle, our results are more consistent with those of Poppen [10], who found that the abduction moment arm of anterior deltoid exceeds that of middle deltoid at large abduction angles of the glenohumeral joint.

In the model, as in the cadaver studies of Liu [44] and Otis [45], the posterior deltoid adducts the shoulder at most angles of abduction of the glenohumeral joint in the scapular plane (Fig. 9C). The adduction moment arm of this muscle is maximum at 0° abduction, and decreases

TABLE I Architectural properties estimated for each musculotendon actuator in the upper-limb model: volume (Vol), maximum musculotendon length (L^{MT}_{max}), minimum musculotendon length (L^{MT}_{min}), physiological cross-sectional area (PCSA), optimal muscle-fiber length (L^{M}_{o}), tendon slack length (L^{T}_{s}), maximum isometric muscle force (F^{M}_{o}), and muscle pennation angle (α). Physiological cross-sectional area was defined as the ratio of muscle volume to optimal muscle-fiber length [35]

Muscle	Abbr.	Vol (cm^3)	L^{MT}_{max} (cm)	L^{MT}_{min} (cm)	PCSA (cm^2)	L^{M}_{o} (cm)	L^{T}_{s} (cm)	F^{M}_{o} (N)	α (deg)
subclavius	SBCL	8.80	7.15	6.28	4.36	2.02	5.07	144.02	0.00
serratus anterior (superior)	SRAs	92.20	12.24	5.84	8.12	11.35	0.27	268.05	0.00
serratus anterior (middle)	SRAm	71.71	19.32	11.23	4.00	17.91	0.75	132.12	0.00
serratus anterior (inferior)	SRAi	194.65	24.89	13.43	8.41	23.15	0.01	277.51	0.00
trapezius (C1–C6)	TRPc	116.23	20.12	9.46	6.24	18.62	0.48	205.95	0.00
trapezius (C7)	TRPc7	77.49	23.21	10.94	3.61	21.44	0.60	119.25	0.00
trapezius (T1)	TRPt1	66.92	21.10	7.76	3.45	19.37	0.32	114.01	0.00
trapezius (T2–T7)	TRPt	197.25	16.92	9.71	12.40	15.91	0.42	409.23	0.00
levator scapulae	LVS	71.92	20.62	12.04	3.78	19.02	0.90	124.78	0.00
rhomboid minor	RMN	117.77	19.00	8.72	6.71	17.55	0.44	221.51	0.00
rhomboid major (T1–T2)	RMJt2	72.27	19.30	7.91	4.14	17.47	0.67	136.48	0.00
rhomboid major (T3–T4)	RMJt3	45.50	19.96	6.93	2.48	18.33	0.24	81.93	0.00
pectoralis minor	PMN	73.14	15.75	8.13	4.87	15.03	0.01	160.55	0.00
pectoralis major (clav)	PMJc	235.09	28.92	8.83	10.38	22.65	0.45	342.46	0.00
pectoralis major (stern)	PMJs	243.34	32.24	12.59	14.68	16.58	9.03	484.35	0.00
pectoralis major (ribs)	PMJr	197.97	34.43	18.37	11.14	17.76	9.58	367.78	0.00
latissimus dorsi (thoracic)	LTDt	183.23	42.14	21.18	5.26	34.87	14.75	173.43	0.00
latissimus dorsi (lumbar)	LTDl	183.23	56.00	35.73	5.27	34.78	19.92	173.88	0.00
latissimus dorsi (illiac)	LTDi	183.23	57.18	39.78	3.80	48.17	10.89	125.52	0.00
deltoid (clavicular)	DLTc	123.48	21.22	9.11	8.41	14.68	1.64	277.48	0.00
deltoid (acromial)	DLTa	376.94	18.22	11.05	56.38	6.69	8.56	1860.52	0.00
deltoid (scapular)	DLTs	292.45	24.14	12.41	17.19	17.02	5.93	567.15	0.00
supraspinatus	SUPR	89.23	18.80	14.45	20.84	4.28	13.03	687.84	0.00
infraspinatus	INFR	225.36	15.29	9.18	33.32	6.76	5.58	1099.61	0.00
subscapularis	SBSC	318.52	13.11	9.40	35.69	8.92	4.94	1177.93	0.00
teres minor	TMN	38.70	12.57	6.00	6.77	5.72	4.55	223.35	0.00
teres major	TMJ	231.40	19.27	10.58	15.59	14.84	5.79	514.51	0.00
coracobrachialis	CRCB	80.01	21.24	14.11	4.55	17.60	4.23	150.05	0.00
triceps brachii (long)	TRClg	290.67	40.29	26.73	19.07	15.24	19.05	629.21	15.00
triceps brachii (medial)	TRCm	92.04	18.95	13.48	18.78	4.90	12.19	619.67	15.00
triceps brachii (lateral)	TRClt	237.28	28.22	22.58	38.45	6.17	19.64	1268.87	15.00
biceps (short)	BICs	182.92	40.46	24.00	13.99	13.07	22.98	461.76	10.00
biceps (long)	BICl	182.92	41.94	26.06	11.91	15.36	22.93	392.91	10.00
brachialis	BRA	265.96	13.01	6.65	25.88	10.28	1.75	853.90	15.00
brachioradialis	BRD	83.19	35.35	21.00	3.08	27.03	6.04	101.58	5.00
supinator	SUP	34.11	9.73	6.09	5.65	6.04	2.48	186.38	0.00
pronator teres	PRNT	80.41	16.61	12.68	17.96	4.48	11.58	592.80	10.00
flexor carpi radialis	FCR	56.97	34.78	28.41	11.16	5.10	27.08	368.41	10.00
flexor carpi ulnaris	FCU	67.66	33.62	27.60	16.99	3.98	27.14	560.70	15.00
extensor carpi radialis long	ECRl	72.87	38.33	29.14	8.13	8.96	26.80	268.42	15.00
extensor carpi radialis brev	ECRb	93.74	34.53	28.06	16.76	5.59	26.87	553.21	20.00
extensor carpi ulnaris	ECU	28.65	33.68	28.93	8.04	3.56	28.18	265.27	20.00

as the glenohumeral abduction angle increases. The model results show further that posterior deltoid abducts the shoulder as the humerus is raised beyond 80° in the scapular plane.

The moment arms of the model infraspinatus and subscapularis agree very well with the results reported by Liu [44] and Hughes [46] (Fig. 9D, subscapularis). At small abduction angles, infraspinatus has a small abduction moment arm, and the model calculations indicate that this muscle may actually adduct the shoulder slightly when the humerus is positioned alongside the torso (not

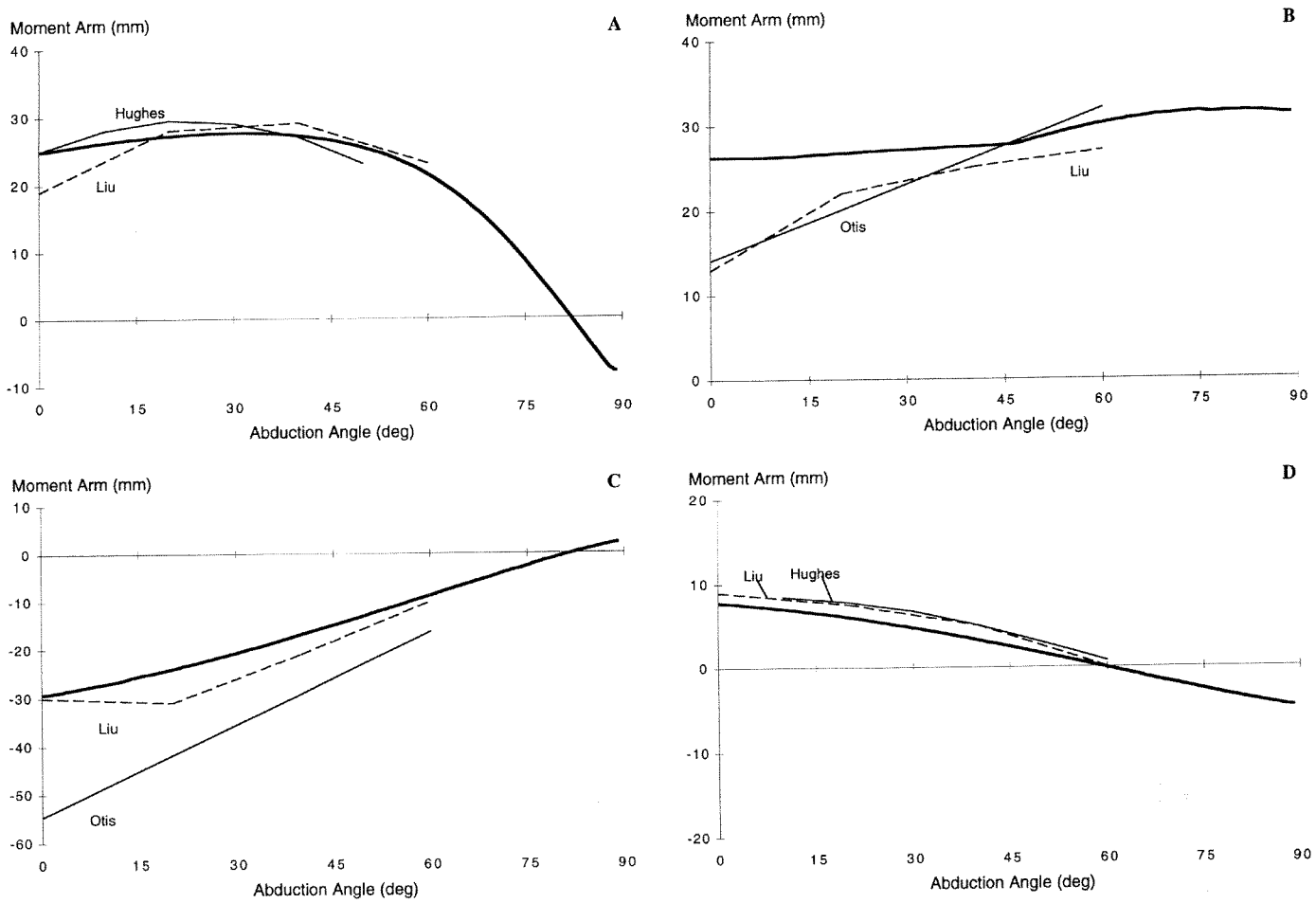

FIGURE 9 Comparison of measured and modeled abduction moment arms for supraspinatus (A), middle deltoid (B), posterior deltoid (C), and subscapularis (D) obtained for elevation of the humerus in the scapular plane. Moment arms are plotted against the abduction angle of the glenohumeral joint in the scapular plane (*i.e.*, the angle between the humerus and the scapula in the scapular plane). 0° abduction is when the humerus is held alongside the torso and the scapula is in its natural resting position with respect to the torso. Abduction moment arms are positive; adduction moment arms are negative. The heavy solid lines are results obtained for the model; the thin solid and dashed lines are results obtained from anatomical studies reported in the literature (Otis [45], Liu [44] and Hughes [46]). The discontinuous slope obtained for middle deltoid in the model (heavy solid line in B) occurs because this muscle loses contact with the humeral head as the humerus is abducted beyond 45° in the scapular plane.

shown in Fig. 9D). As glenohumeral abduction angle increases, however, infraspinatus' role is clearly one of abduction. Subscapularis acts both as an abductor and an adductor in the model, although its moment arm remains relatively small throughout the range of shoulder abduction movement (Fig. 9D). This behavior of the model is also consistent with that observed from experiment [44, 46].

Elbow

The moment arms calculated in the model for humeroulnar flexion-extension and forearm pronation-supination agree quite well with the results of the cadaver studies. With the forearm in neutral rotation, brachioradialis has the largest flexion moment arm, followed by biceps, brachialis, extensor carpi radialis longus, and pronator teres. The flexion moment arm for brachioradialis is about 6 times greater than that for pronator teres at all elbow flexion angles. Peak flexion moment arm for the model brachioradialis is 75 mm at 120° of elbow flexion, which is higher than the mean maximum value of 60 mm measured by Murray [17] (Fig. 10A). Biceps flexion moment arm in the model is also higher than the values reported by Murray [17]. For example, peak flexion moment arm is 45 mm in the model, compared with a mean peak value of 40 mm obtained for the cadavers (Fig. 10B).

Lemay [18] found that the two portions of extensor carpi radialis had very different functions, with longus causing flexion of the elbow and brevis causing extension throughout the range of elbow joint movement. The model extensor carpi radialis longus flexes the elbow throughout the range of elbow movement, whereas the model extensor carpi radialis brevis can act both as an elbow extensor and an elbow flexor, depending on the flexion angle of this joint (not shown in Fig. 10).

In the model, as in the cadavers tested by Murray [17], triceps has the largest extension moment arm at the elbow (Fig. 10C). The peak extension moment arm calculated in the model is 26 mm, which is very close to the mean values measured for the medial, lateral, and long heads of triceps [17]. Extensor carpi ulnaris also acts to extend the elbow, but its moment arm is significantly smaller than that of triceps (not shown in Fig. 10). In the model, flexor carpi radialis and flexor carpi ulnaris can each flex and extend the elbow depending on the flexion angle of the joint; near full extension, these muscles both act as extensors, whereas at flexion angles greater than 105° they both act as flexors (not shown in Fig. 10). These results agree, at least qualitatively, with those reported by An [41].

Consistent with the anatomical measurements of Murray [17], pronation-supination moment arms for all the muscles crossing the elbow in the model are much smaller than the corresponding moment arms for flexion-extension. For example, peak supination moment arm for the model biceps is 14 mm, compared with a peak flexion moment arm of 45 mm (*cf.* heavy solid lines in Figs. 10B and D). The biceps and supinator have the largest supination moment arms in the model, whereas pronator teres has the largest pronation moment arm (not shown in Fig. 10). Brachioradialis shares its responsibilities as pronator and supinator almost equally: when the forearm is supinated, brachioradialis acts as a pronator, but when the forearm is pronated, this muscle acts as a supinator (not shown in Fig. 10).

Wrist

The flexion-extension moment arms of the wrist muscles in the model vary with wrist position. In agreement with the results reported by Loren [20], the extension moment arms of the model extensor carpi radialis brevis (ECRB) and extensor carpi radialis longus (ECRL) are smallest in flexion and increase with progressive wrist extension (Figs. 11A and B). Also, the extension moment arms for ECRB and ECRL are larger than that for extensor carpi ulnaris (ECU) at most wrist flexion angles in the model. Peak flexion moment arms for the model flexor carpi radialis (FCR) and flexor carpi

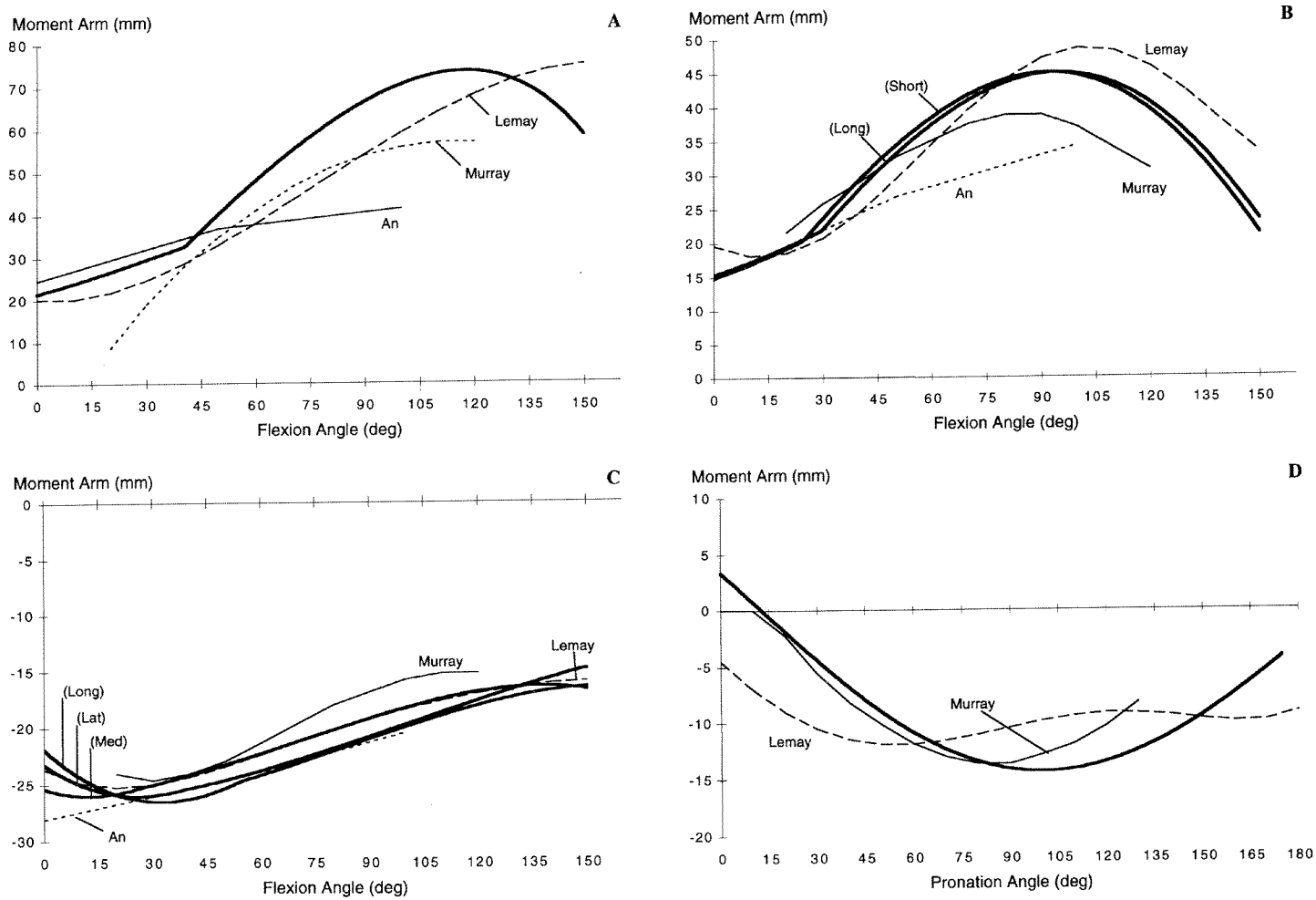

FIGURE 10 Comparison of measured and modeled elbow flexion moment arms for brachioradialis (A), biceps brachii (B), and triceps brachii (C). Measured and modeled forearm pronation moment arms for biceps brachii are given in (D). 0° flexion is when the elbow is fully extended; 0° pronation is when the forearm is fully supinated. Flexion-extension moment arms were computed with the upper arm adjacent to the torso, the forearm in neutral pronation, and the wrist in a neutral position. Pronation-supination moment arms were computed with the elbow flexed to 90° and the wrist in a neutral position. Flexion and pronation moment arms are positive; extension and supination moment arms are negative. The heavy solid lines are results obtained for the model; the thin solid, dashed, and dotted lines are results obtained from anatomical studies reported in the literature (An [41], Murray [17], Lemay [18]). The discontinuous slopes obtained for brachioradialis and biceps brachii in the model (heavy solid lines in A and B, respectively) occur because these muscles wrap around the distal humerus as the elbow extends beyond 40° and 30°, respectively.

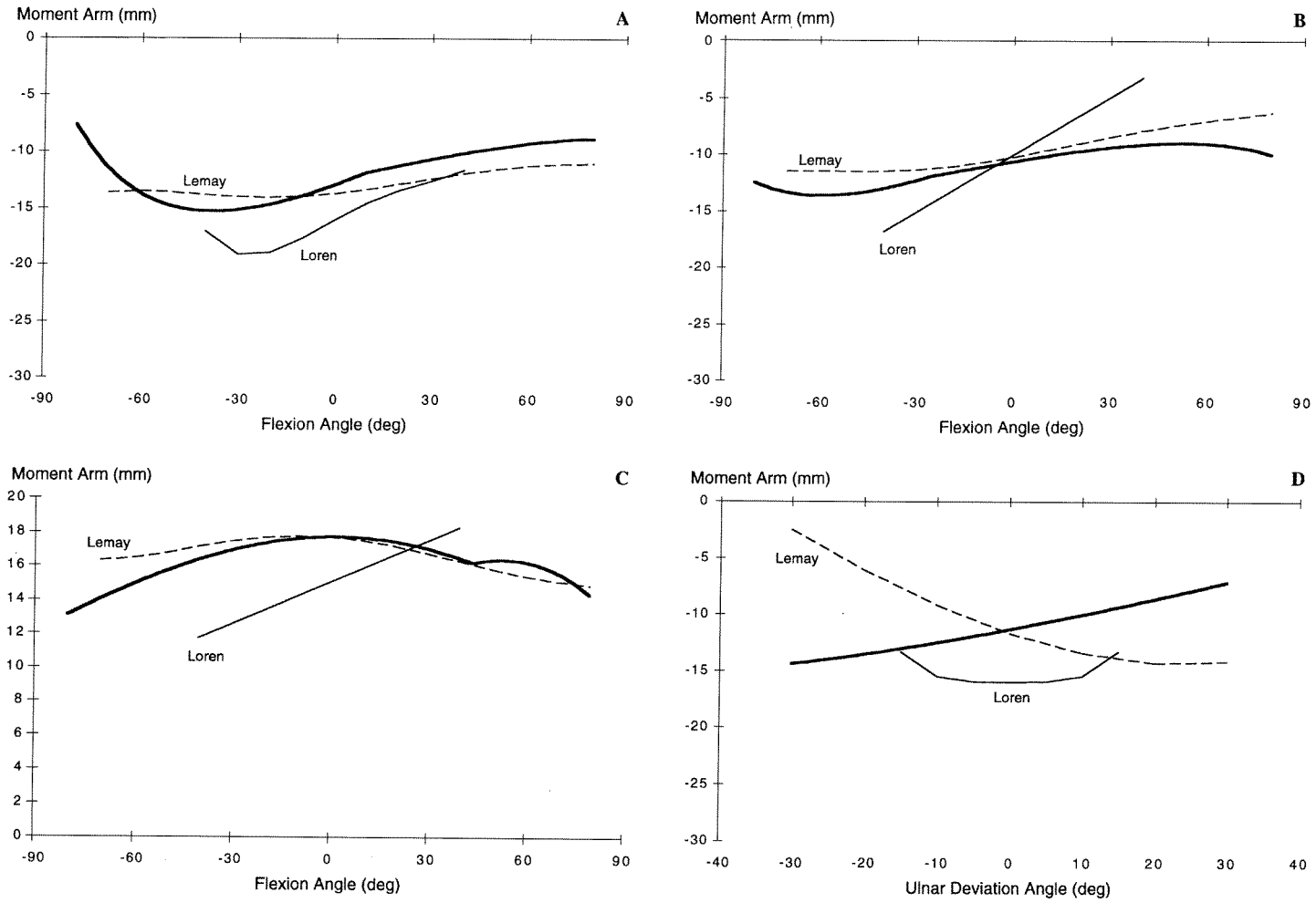

FIGURE 11 Comparison of measured and modeled wrist flexion moment arms for extensor carpi radialis brevis (A), extensor carpi radialis longus (B), and flexor carpi radialis (C). Measured and modeled wrist ulnar deviation moment arms for extensor carpi radialis brevis are given in (D). 0° flexion and 0° ulnar deviation defines the neutral position of the wrist. Flexion-extension moment arms were computed with the elbow flexed to 90° and the forearm in neutral pronation. Flexion and ulnar deviation moment arms are positive; extension and radial deviation moment arms are negative. The heavy solid lines are results obtained for the model; the thin solid and dashed lines are results obtained from anatomical studies reported in the literature (Loren [20], Lemay [18]). The discontinuous slope obtained for flexor carpi radialis in the model (heavy solid line in C) occurs because this muscle loses contact with the carpal bones as the wrist flexes beyond 45°.

ulnaris (FCU) are about 18 mm, and the peak for each muscle occurs with the wrist in neutral (Fig. 11C, FCR). This result is noticeably different from that reported by Loren [20], who found that the peak flexion moment arm for each of these muscles occurs when the wrist is fully flexed. The model results, however, are consistent with those given by Lemay [18] (*cf.* heavy solid and dashed lines in Fig. 11C).

The model ECRB, ECRL, and FCR all act as radial deviators of the wrist. Peak radial deviation moment arms for ECRB and ECRL in the model are 15 mm and 16 mm, respectively, which agree well with the values measured by Loren [20] (*cf.* heavy and thin solid lines in Fig. 11D). ECU and FCU act as ulnar deviators of the wrist throughout the range of radial-ulnar deviation movement in the model, with the ulnar deviation moment

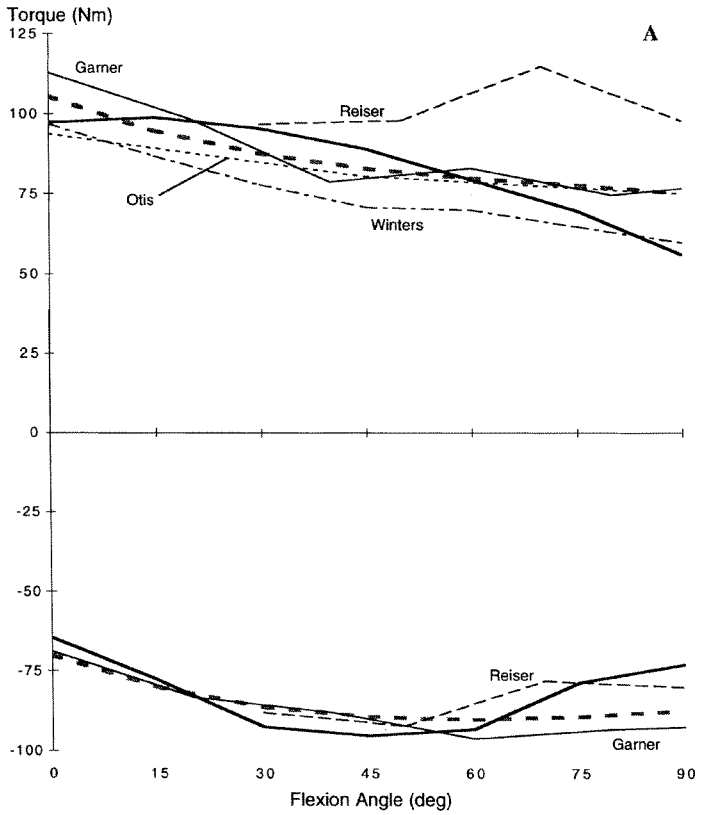

FIGURE 12 Comparison of measured and calculated joint torques for shoulder flexion-extension (A), shoulder abduction-adduction (B), and shoulder internal-external rotation (C). 0° abduction and 0° flexion is when the humerus is held alongside the torso; 0° internal rotation is when the humerus is held in neutral rotation. Shoulder flexion-extension torques were computed with the shoulder held in 0° abduction and 0° internal rotation and with the elbow flexed to 60°. Shoulder abduction-adduction torques were calculated for elevation of the humerus in the scapular plane, with the shoulder held in neutral rotation and the elbow flexed to 60°. Abduction-adduction torques are plotted against the glenohumeral angle, which is the angle between the humerus and the scapula in the scapular plane. Shoulder internal-external rotation torques were computed with the shoulder abducted 60° in the scapular plane and the elbow flexed to 60°. The heavy solid lines are results obtained for the model. The thin dashed, dot-dashed, and dotted lines are experimental measurements reported in the literature (see below). The thin solid lines are the mean of the experimental measurements recorded for the three subjects who participated in the present study (Garner [39]). The thick grey dashed lines are the mean of all the experimental results. Flexion, abduction, and internal rotation torques are positive; extension, adduction, and external rotation torques are negative. Measured maximum isometric torques were obtained from the following literature studies: Otis [48], Reiser [59] and Winters [47] for shoulder flexion-extension; Otis [48] and Reiser [59] for shoulder abduction-adduction; and Engin [60] and Otis [48] for shoulder internal-external rotation.

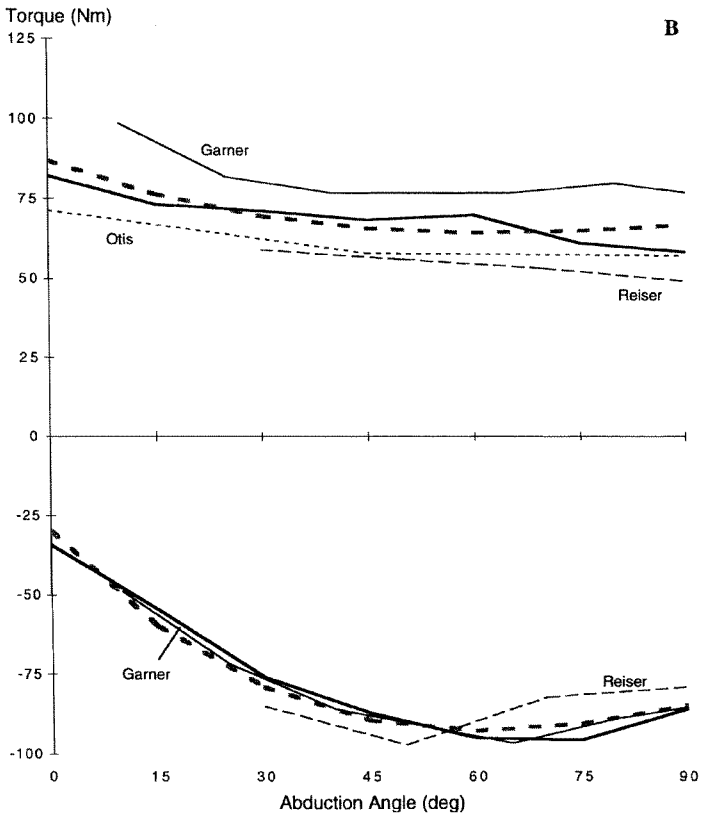

arm of ECU being much larger (not shown in Fig. 11).

Joint Torques

Shoulder

Maximum shoulder torques vary with flexion, abduction, and internal rotation of the shoulder. Shoulder flexion torque in the model is close to 100 Nm with the humerus positioned alongside the torso, and it decreases almost linearly with increasing shoulder flexion (Fig. 12A).

These results are consistent with measurements obtained from our subjects as well as experimental data reported by Winters [47] and Otis [48]. The model and the subjects are equally as strong in flexion and extension, except when the humerus is positioned alongside the torso. Peak extension torque in the model is around 90 Nm, compared with 100 Nm for flexion (*cf.* heavy solid lines in Fig. 12A).

The model and subjects are also almost equally as strong in abduction and adduction. Peak shoulder abduction torque in the model is about 80 Nm and occurs with the humerus positioned alongside the torso (Fig. 12B). Peak adduction torque is about 90 Nm, but maximum torque for adduction occurs only when the glenohumeral abduction angle is at 75°; when the humerus is held alongside the torso, adduction torque in the model and the subjects is relatively small (about 30 Nm). For the model and the subjects, there is greater variation in adduction torque than in abduction torque as the humerus is elevated relative to the scapula in the scapular plane (*i.e.*, adduction

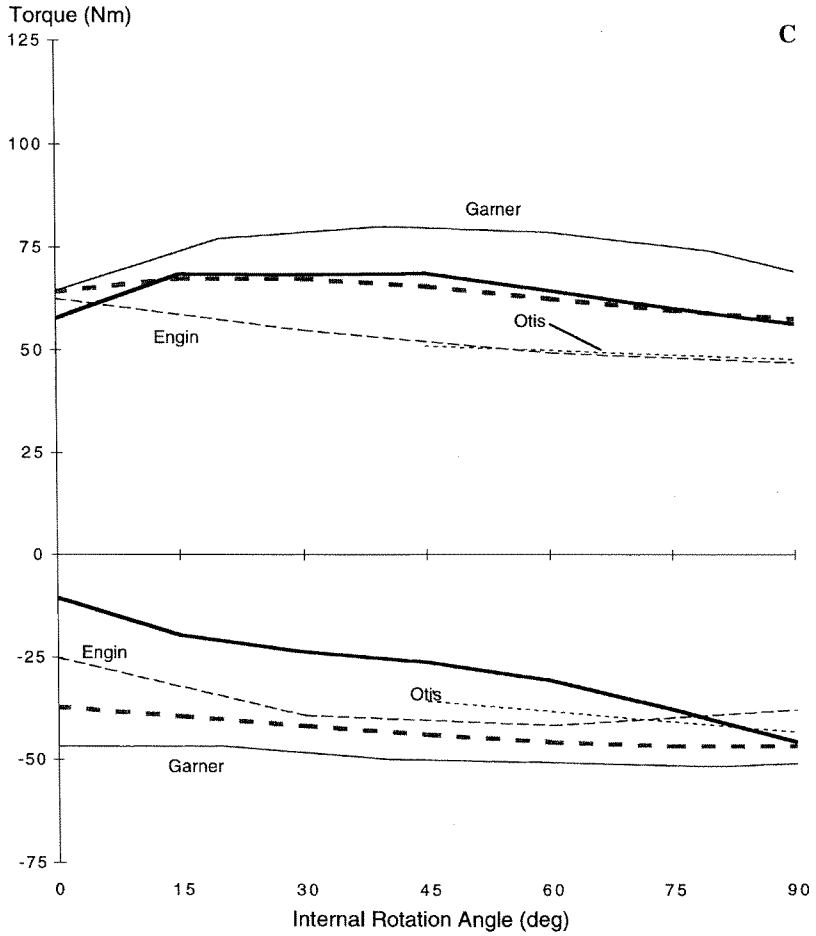

FIGURE 12 (Continued).

torque varies from about 30 Nm to 90 Nm, whereas abduction torque varies from about 85 Nm to 70 Nm over the full range of shoulder abduction; compare heavy solid and dashed lines in Fig. 12B).

Maximum torques for internal and external rotation about the long axis of the humerus are smaller than those for either flexion-extension or abduction-adduction. Peak torque during internal rotation for the model is about 70 Nm, which agrees well with the value obtained from experiment (*cf.* heavy solid and dashed lines in Fig. 12C). Peak torques generated during external rotation are much lower than those produced during internal rotation. There is some discrepancy between the maximum external rotation torques developed in the model and those measured in people, particularly near full external rotation of the shoulder (0° in Fig. 12C for external rotation). This result is due to failure of our parameter estimation method to find a suitable set of values of F_o^M, L_o^M, and L_s^T for each actuator which (1) produces a good match between the calculated and measured values of maximum isometric joint torque, and (2) satisfies the constraints imposed by the calculated values of muscle volumes and maximum and minimum musculotendon lengths.

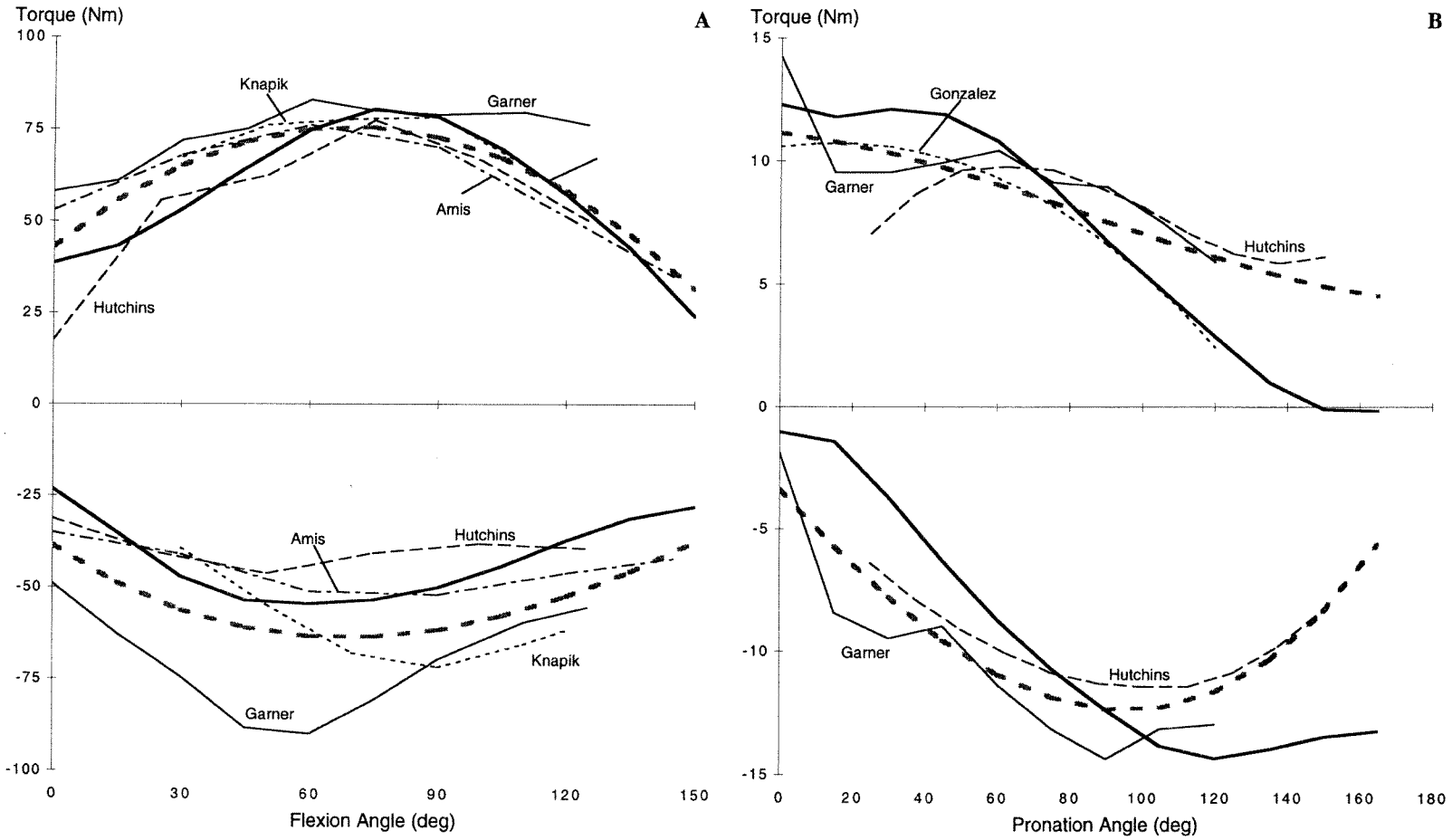

FIGURE 13 Comparison of measured and calculated maximum isometric joint torques for elbow flexion-extension (A) and forearm pronation-supination (B). 0° flexion is when the elbow is fully extended; 0° pronation is when the forearm is fully supinated. Elbow flexion-extension torques were computed with the shoulder held alongside the torso and the forearm fully supinated. Forearm pronation-supination torques were computed with the elbow flexed to 90° and the shoulder positioned alongside the torso. The heavy solid lines are results obtained for the model. The thin dashed, dot-dashed, and dotted lines are experimental measurements reported in the literature (see below). The thin solid lines are the mean of the experimental measurements recorded for the three subjects who participated in the present study (Garner [39]). The thick grey dashed lines are the mean of all the experimental results. Flexion and pronation torques are positive; extension and supination torques are negative. Measured maximum isometric torques were obtained from: Amis [61], Knapik [62] and Hutchins [50] for elbow flexion-extension; and Hutchins [50] and Gonzalez [63] for forearm pronation-supination.

Elbow

Maximum torques at the elbow vary considerably throughout the range of joint motion for both flexion-extension and pronation-supination. Mean peak torques for elbow flexion-extension are lower than those produced during either flexion-extension or abduction-adduction of the shoulder (*cf.* Fig. 13A with Figs. 12A and B). Peak elbow flexion and extension torques for the model are respectively 80 Nm and 55 Nm, compared with corresponding values of 75 Nm and 65 Nm developed by the subjects for flexion and extension, respectively (*cf.* heavy solid and dashed lines in Fig. 13A).

Maximum elbow pronation-supination torques are much lower than those for either flexion or extension. For the model and the subjects, peak pronation torque occurs with the forearm fully supinated, and maximum torque decreases with increasing pronation. Conversely, peak supination torque occurs with the forearm almost fully pronated, with maximum torque decreasing as forearm supination increases (Fig. 13B).

Wrist

There is considerable variability in the maximum torques measured for flexion-extension and radial-ulnar deviation at the wrist. For example, Delp [49] reported peak wrist flexion torques of around 11 Nm, whereas our own measurements and the data recorded by Hutchins [50] show peak values that are approximately twice as large (Fig. 14A, Flexion). For the model and the subjects, peak flexion torques are significantly higher than peak extension torques. Peak torque developed by the

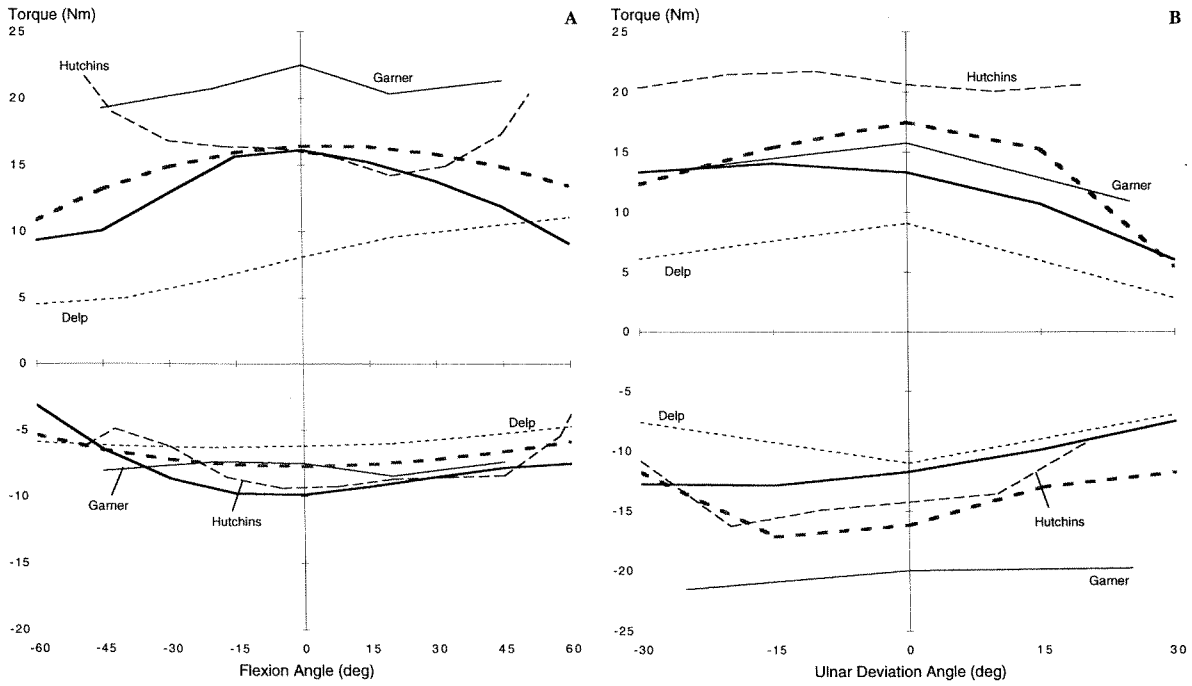

FIGURE 14 Comparison of measured and calculated maximum isometric joint torques for wrist flexion-extension (A) and wrist radial-ulnar deviation (B). 0° flexion and 0° ulnar deviation defines the neutral position of the wrist. Wrist flexion-extension and radial-ulnar deviation torques were computed with the elbow flexed to 90° and the forearm in neutral pronation. The heavy solid lines are results obtained for the model. The thin dashed and dotted lines are experimental measurements reported in the literature (see below). The thin solid lines are the mean of the experimental measurements recorded for the three subjects who participated in the present study (Garner [39]). The thick grey dashed lines are the mean of all the experimental results. Flexion and ulnar deviation torques are positive; extension and radial deviation torques are negative. Measured maximum isometric torques were obtained from Hutchins [50] and Delp [49] for wrist flexion-extension and radial-ulnar deviation.

model for flexion is 17 Nm, compared with only 10 Nm for extension (*cf.* heavy solid lines in Fig. 14A). Interestingly, the model and the subjects are almost equally as strong in flexion-extension as in radial-ulnar deviation. Peak radial and ulnar deviation torques calculated for the model are around 15 Nm, which is in the range of the values obtained for flexion and extension (*cf.* heavy solid lines in Figs. 14A and B).

DISCUSSION

This paper presents a model of the musculoskeletal geometry and architectural properties of all the major muscles crossing the shoulder, elbow, and wrist in the human upper limb. The model is based on high-resolution medical images of the muscles and bones obtained from the VHM dataset. The musculoskeletal geometry assumed in the model was verified by comparing computed muscle moment arms with *in vitro* moment-arm data reported in the literature. Measurements of maximum isometric muscle torques obtained from human subjects were also used to estimate the architectural properties of each musculotendon actuator in the model.

One of the main contributions of this work is that sufficient information is given to enable the reader to reconstruct a mathematical model of the upper limb from scratch. Specifically, the entire musculoskeletal model of the VHM upper limb can be reconstructed using the data given in Tabs. I and IV of this paper, along with the information presented in a companion paper [26] which describes the kinematic structure of the model.

Our model for upper-limb musculoskeletal geometry is more general and more complete than what has been presented to date. Amis [37], An [41], Wood [30] and Pigeon [24] reported moment arms for various muscles crossing the shoulder, elbow, and wrist, but the paths of the muscles cannot be reconstructed from the information given in these papers. Amis [15] also reported direction cosines of the arm muscles for various positions of the elbow joint, but with the shoulder held fixed. Muscles such as the long head of triceps brachii and the short head of biceps brachii cross both the shoulder and elbow, so the data given by Amis [15] do not show how the muscle lines-of-action change as the orientation of the humerus changes relative to the scapula in all three planes. The geometric parameters listed in Table IV of the Appendix applies for *all* configurations of the shoulder, elbow, and wrist, so it is possible to determine from our model how the lines-of-action and moment arms of the muscles at a primary joint change as the configuration of a neighboring joint changes.

Previous workers have developed models of the shoulder girdle [12, 29, 51], elbow [15, 16], and wrist [19–21] (see Tab. II). Some workers have also developed models which combine two or more of these joints into a single model of the upper limb (*e.g.*, Seireg [22], Raikova [23], Yamaguchi [52] and Lemay [18]). No one, to our knowledge, has presented a model that includes all the major articulations of the shoulder girdle, elbow, and wrist. The model described by Seireg [22], although perhaps the most detailed to date, has a number of limitations. First, the model does not include the scapulothoracic articulation. Second, the muscle paths, which are modeled as straight lines, are based on crude descriptions of muscle and bone geometry reported in anatomy textbooks. Third, the kinematic structure of the model was derived from an amalgamation of joint anatomical measurements obtained from various cadaveric specimens. By comparison, our model of the upper limb takes into account all the major muscles and joints from the shoulder girdle down to the wrist, and it is based on a high-resolution set of muscle and bone geometric data obtained from a *single* specimen: the VHM cadaver. The model uses 13 degrees of freedom to describe the relative positions and orientations of seven bones (clavicle, scapula, humerus, radius, ulna, carpal bones, and hand), and it is actuated by 42 muscle bundles which represent the actions of 26 muscle groups (see Tab. III).

The paths of the upper-limb muscles in our model are also given more precisely than in

TABLE II Survey of the kinematic complexities of upper-limb models reported in the literature. Criteria used to compare different models are: (1) whether or not the model is three-dimensional (3D); (2) joints included in the model: sternoclavicular (SC), acromioclavicular (AC), scapulothoracic (ST), glenohumeral (GH), humeroulnar (HU), radioulnar (RU), radiocarpal flexion-extension (RC–FE), and radiocarpal radial-ulnar deviation (RC–RU); and (3) number of degrees of freedom included in the model (DOF's)

Study	3D	SC	AC	ST	GH	HU	RU	RC–FE	RC–RU	DOFs
Bassett [40]	√	–	–	–	√	–	–	–	–	3
Poppen [10]	–	–	–	–	√	–	–	–	–	1
Hogfors [29]	√	√	√	√	√	–	–	–	–	9
Van der Helm [51]	√	√	√	√	√	–	–	–	–	9
Wood [30]	√	√	√	–	√	√	√	–	–	11
Seireg [22]	√	√	√	–	√	√	√	√	√	13
Pigeon [24]	–	–	–	–	√	√	–	√	–	3
Raikova [23]	√	–	–	–	√	√	√	√	√	7
Yamaguchi [52]	√	–	–	–	√	√	√	–	–	5
Amis [61]	√	–	–	–	–	√	–	–	–	2
An [41]	√	–	–	–	–	√	–	–	–	1
Murray [17]	√	–	–	–	–	√	√	–	–	2
Gonzalez [16]	√	–	–	–	–	√	√	–	–	2
Lemay [18]	√	–	–	–	–	√	√	√	√	4
Hutchins [50]	√	–	–	–	–	√	√	√	√	4
Buchanan [19]	√	–	–	–	–	√	√	√	√	4
Loren [20]	√	–	–	–	–	–	–	√	√	2
Gonzalez [21]	√	–	–	–	–	–	–	√	√	1
Current Model	√	√	√	√	√	√	√	√	√	13

previous studies. Three factors contribute to this increased level of accuracy: first, our model of musculoskeletal geometry is based directly on high-resolution images of the muscles and bones obtained from the VHM dataset; second, the paths of the muscles in the model were fitted directly to the centroidal paths of the muscles in the VHM cadaver; and third, our Obstacle-set method for modeling muscle paths allows each muscle to move freely over the neighboring muscles and bones during joint movement. Previous studies have introduced effective attachment sites or *via* points at specific locations along the centroidal path of a muscle [5, 7, 17] (see Tab. III). Since these muscle *via* points remain fixed relative to the bones even as the joints move, muscle-path models that use only fixed *via* points can yield discontinuous values of muscle length and moment arm (see Garner [33] for details). Our Obstacle-set method accounts not only for the interaction between a muscle and its neighboring anatomical constraint, but also for the way in which this interaction changes as the bones move relative to each other.

There are also some limitations of the approach we have taken to model the geometry and architectural properties of the muscles in the upper limb. Perhaps most significantly, only a limited amount of information is available to validate the model calculations. The experimental studies reported in the literature do not fully describe the variation of the moment arms and joint torques of the muscles crossing the shoulder, elbow, and wrist. For example, Otis [45] and Liu [44] recorded the moment arms of the rotator cuff muscles for abduction of the humerus in the scapular plane, and these results were used to verify the accuracy of the abduction moment arms of the rotator cuff muscles in the model (Fig. 9). Unfortunately, since no experimental data are available for the moment arms of these muscles for flexion-extension and internal-external rotation of the shoulder, the model calculations could not be verified for these degrees of freedom as well. More data are also needed to describe the muscle torque-angle relations at the shoulder, elbow, and wrist. For example, Delp [49] recorded the maximum

TABLE III Survey of the musculoskeletal complexities of upper-limb models reported in the literature. Criteria used to compare different models are: (1) number of muscle groups (# muscles) and number of muscle bundles (# Bundles) included in the model, (2) method used to model the muscle-path geometry (see legend below), and (3) musculotendon parameters included in the model: physiological cross-sectional area (PCSA), maximum isometric force (F_o^M), optimal muscle-fiber length (L_o^M), tendon slack length (L_s^T), and muscle pennation angle (α)

Study	# Muscles	# Bundles	Geometry	PCSA	F_o^M	L_o^M	L_s^T	α
Bassett [40]	12	15	PD		?	?		
Poppen [10]	5	7	PD		?			
Hogfors [29]	21	33	GS	√	√	–	–	–
Van der Helm [51]	16	101	GS	√	√	–	–	–
Wood [30]	22	30	PD	√	–	–	–	–
Seireg [22]	24	34	SL	–	–	–	–	–
Pigeon [24]	13	13	PY	–	–	–	–	–
Raikova [23]	30	37	SV	–	–	–	–	–
Yamaguchi [52]	30	30	SV	√	–	–	–	–
Amis [61]	5	5	DC	√	√	–	–	√
An [41]	3	3	DC	√	√	√	–	–
Murray [17]	5	5	SV	–	–	–	–	–
Gonzalez [16]	8	8	SV	√	√	√	√	√
Lemay [18]	34	37	PY	√	√	√	√	√
Hutchins [50]	12	12	SV	√	√	√	√	√
Buchanan [19]	13	16	PD	√	√	–	–	–
Loren [20]	5	5	PY	–	√	√	√	√
Gonzalez [21]	15	15	SV	–	√	√	–	–
Current Model	26	42	OS	√	√	√	√	√

Legend: Muscle Path Geometry
PD – Moment arms were calculated as the Perpendicular Distance between the path of the muscle and the joint center.
GS – Centroid paths of muscles were approximated as an elastic band wrapping around simple Geometric Shapes representing underlying obstacles.
SL – Paths of muscles were modeled as Straight Lines joining the origin and insertion sites.
SV – Paths of muscles were modeled as Straight or curved line segments connecting *via* points that remain fixed on the bones.
DC – Moment arms were computed based on the Direction Cosines of unit vectors tangent to the muscle path at the point of attachment of the muscle to bone.
PY – Moment arms were represented by polynomial functions of joint angles.
OS – Centroid paths of the muscles were approximated using the Obstacle-Set method [33].

isometric torques developed by the wrist muscles for flexion-extension and radial-ulnar deviation of the wrist, but no data are available for combined movements of this joint. Since the upper limb may be configured in many different ways, it is understandably difficult to obtain measurements of moment arms and joint torques which account for all possible positions of the shoulder, elbow, and wrist.

A second limitation of our work is that the method used to estimate musculotendon properties in the model may not have yielded unique results. Values of maximum isometric mucle force, optimum muscle-fiber length, and tendon slack length were obtained by minimizing the differences between the calculated and measured values of joint torques. Since the bones and muscles of the upper limb comprise a mechanically redundant system, it is possible for the above requirement to be satisfied by more than one set of musculotendon parameters. The values given in Table I should nevertheless approximate the properties of the upper-limb muscles in the VHM cadaver because (1) the results of a large number of joint torque simulations were included in the optimization calculations; (2) the model simulations were performed over a large region of the configuration space of the upper limb; and (3) the architectural properties of each actuator were constrained by the calculated values of muscle volume and maximum and minimum musculotendon actuator lengths.

Recommendations for Future Research

Upper-limb modeling studies cannot progress beyond the current state without more complete descriptions of musculotendon architecture. Measurements of muscle volume and PCSA are available for most of the muscles of the upper limb [32, 35, 42, 43, 53–56]. Some data are also available to specify fiber lengths and pennation angles, but this information is restricted to the muscles of the forearm and hand [35, 43, 55]. Very few data are available to specify fiber lengths and pennation angles for the more proximal muscles of the arm and torso [57], and virtually no information has been published on tendon slack lengths for any of the actuators in the upper limb.

A larger experimental database is also needed to validate the calculations obtained from a model of the upper limb. Many studies have measured the moment arms and joint torques produced by the muscles crossing the elbow and wrist [17, 19, 49, 58], but relatively little has been done to describe the variation of the moment arms and joint torques of the muscles crossing the shoulder. Otis [45] and Liu [44] measured the moment arms of the deltoid and rotator cuff muscles for elevation of the humerus in the scapular plane, but the corresponding values for flexion and internal rotation of the shoulder were not recorded. Wood [30] and Bassett [40] measured the moment arms of the shoulder muscles about all three joint axes of rotation, but these data were obtained for only one position of the arm. Winters [47] recorded the maximum isometric joint torques for flexion and abduction of the shoulder, but not for internal rotation. More data are also needed to specify how the net muscle torque developed at a primary joint is affected by changes in the configuration of a neighboring joint; for example, how shoulder flexion and shoulder abduction torques are affected by changes in elbow and forearm configuration.

Acknowledgments

Partial funding for this work was provided by NASA Grants NGT-51025 and NAG9-805. We thank the National Library of Medicine for making available to us the Visible Human Project dataset. Support provided by the Visualization Laboratory at The University of Texas Center for High Performance Computing is also gratefully acknowledged.

References

[1] Hatze, H. (1980). Neuromusculoskeletal control systems modeling – A critical survey of recent developments. *IEEE Transactions on Automatic Control*, **AC-25**, 375–385.

[2] Zajac, F. E. and Gordon, M. E. (1989). Determining muscle's force and action in multiarticular movement. *Exercise and Sport Sciences Reviews*, **17**, 187–230.

[3] Loeb, G. E. and Levine, W. S. (1990). Linking musculoskeletal mechanics to sensorimotor neurophysiology. In: Winters, J. M. and Woo, S. L. (Eds.), *Multiple Muscle Systems*, Springer-Verlag, pp. 165–181.

[4] Brand, R. A., Crowninshield, R. D., Wittstock, C. E., Pedersen, D. R., Clark, C. R. and van Krieken, F. M. (1982). A model of lower-extremity muscular anatomy. *Journal of Biomechanical Engineering*, **104**, 304–310.

[5] Delp, S. L., Loan, J. P., Hoy, M. G., Zajac, F. E., Topp, E. L. and Rosen, J. M. (1990). An interactive graphics-based model of the lower extremity to study orthopaedic surgical procedures. *IEEE Transactions on Biomedical Engineering*, **37**, 757–767.

[6] White, S. C., Yack, J. H. and Winter, D. A. (1989). A three-dimensional musculoskeletal model for gait analysis. Anatomical variability estimates. *Journal of Biomechanic*, **22**, 885–893.

[7] Hoy, M. G., Zajac, F. E. and Gordon, M. E. (1990). A musculoskeletal model of the human lower extremity: The effect of muscle, tendon, and moment arm on the moment-angle relationship of musculotendon actuators at the hip, knee, and ankle. *Journal of Biomechanics*, **23**, 157–169.

[8] Kepple, T. M., Sommer, H. J., Siegel, K. L. and Stanhope, S. J. (1998). A three-dimensional musculoskeletal database for the lower extremities. *Journal of Biomechanics*, **31**, 77–80.

[9] DeLuca, C. J. and Forrest, W. J. (1973). Force analysis of individual muscles acting simultaneously on the shoulder joint during isometric abduction. *Journal of Biomechanics*, **6**, 385–393.

[10] Poppen, N. K. and Walker, P. S. (1978). Forces at the glenohumeral joint in abduction. *Clinical Orthopaedics and Related Research*, **135**, 165–170.

[11] Hogfors, C., Peterson, B., Sigholm, G. and Herberts, P. (1991). Biomechanical model of the human shoulder joint–II. The shoulder rhythm. *Journal of Biomechanics*, **24**, 699–709.

[12] Karlsson, D. and Peterson, B. (1992). Towards a model for force predictions in the human shoulder. *Journal of Biomechanics*, **25**, 189–192.

[13] Van der Helm, F. C. T. (1994). Analysis of the kinematic and dynamic behavior of the shoulder mechanism. *Journal of Biomechanics*, **27**, 527–550.

[14] Happee, R. and Van der Helm, F. C. T. (1995). The control of shoulder muscles during goal directed movements, an inverse dynamic analysis. *Journal of Biomechanics*, **28**, 1179–1191.

[15] Amis, A. A., Dowson, D. and Wright, V. (1980a). Elbow joint force predictions for some strenuous isometric actions. *Journal of Biomechanics*, **13**, 765–775.
[16] Gonzalez, R. V., Hutchins, E. L., Barr, R. E. and Abraham, L. D. (1996). Development and evaluation of a musculoskeletal model of the elbow joint complex. *Journal of Biomechanical Engineering*, **118**, 32–40.
[17] Murray, W. M., Delp, S. L. and Buchanan, T. S. (1995). Variation of muscle moment arms with elbow and forearm position. *Journal of Biomechanics*, **28**, 513–525.
[18] Lemay, M. A. and Crago, P. E. (1996). A dynamic model for simulating movements of the elbow, forearm, and wrist. *Journal of Biomechanics*, **29**, 1319–1330.
[19] Buchanan, T. S., Moniz, M. J., Dewald, J. P. A. and Zev Rymer, W. (1993). Estimation of muscle forces about the wrist joint during isometric tasks using an EMG coefficient method. *Journal of Biomechanics*, **26**, 547–560.
[20] Loren, G. J., Shoemaker, S. D., Burkholder, T. J., Jacobson, M. D., Friden, J. and Lieber, R. L. (1996). Human wrist motors: Biomechanical design and application to tendon transfers. *Journal of Biomechanics*, **29**, 331–342.
[21] Gonzalez, R. V., Buchanan, T. S. and Delp, S. L. (1997). How muscle architecture and moment arms affect wrist flexion–extension moments. *Journal of Biomechancis*, **30**, 705–712.
[22] Seireg, A. and Arvikar, R. J. (1989). Modeling of the musculoskeletal system for the upper and lower extremities. In: *Biomechanical Analysis of the Musculoskeletal Structure for Medicine and Sports*, Hemisphere Publisher, pp. 99–128.
[23] Raikova, R. (1992). A general approach for modelling and mathematical investigation of the human upper limb. *Journal of Biomechanics*, **25**, 857–867.
[24] Pigeon, P., Yahia, L. and Feldman, A. G. (1996). Moment arms and lengths of human upper limb muscles as functions of joint angles. *Journal of Biomechanics*, **29**, 1365–1370.
[25] Putnam, C. A. (1993). Sequential motions of body segments in striking and throwing skills: descriptions and explanations. *Journal of Biomechanics*, **26**, 125–135.
[26] Garner, B. A. and Pandy, M. G. (1999). A kinematic model of the upper limb based on the Visible Human Project (VHP) image dataset. *Computer Methods in Biomechanics and Biomedical Engineering*, **2**, 107–124.
[27] Lorensen, W. E. and Cline, H. E. (1987). Marching Cubes: A high resolution 3D surface construction algorithm. *Computear Graphics*, **21**, 163–169.
[28] Schroeder, W. J., Zarge, J. A. and Lorensen, W. E. (1992). Decimation of triangle meshes. *Computer Graphics*, **26**, 65–70.
[29] Hogfors, C., Sigholm, G. and Herbets, P. (1987). Biomechanical model of the human shoulder–I. Elements. *Journal of Biomechanics*, **20**, 157–166.
[30] Wood, J. E., Meek, S. G. and Jacobsen, S. C. (1989). Quantitation of human shoulder anatomy for prosthetic arm control–II. Anatomy matrices. *Journal of Biomechanics*, **22**, 309–325.
[31] Van der Helm, F. C. and Veenbaas, R. (1991). Modelling the mechanical effect of muscles with large attachment sites: Application to the shoulder mechanism. *Journal of Biomechanics*, **24**, 1151–1163.
[32] Johnson, G. R., Spalding, D., Nowitzke, A. and Bogduk, N. (1996). Modelling the muscles of the scapula: Morphometric and coordinate data and functional implications. *Journal of Biomechanics*, **29**, 1039–1051.
[33] Garner, B. A. and Pandy, M. G. (2000). The Obstacle-set Method for representing muscle paths in musculoskeletal models. *Computer Methods in Biomechanics and Biomedical Engineering*, **3**, 1–30.
[34] Zajac, F. E. (1989). Muscle and tendon: properties, models, scaling, and application to biomechanics and motor control. *CRC Critical Reviews in Biomedical Engineering* (Edited by Bourne, J. R.), Williams and Wilkins, Baltimore, **17**, 187–230.
[35] Lieber, R. L., Jacobson, M. D., Fazeli, B. M., Abrams, R. A. and Botte, M. J. (1992). Architecture of selected muscles of the arm and forearm: Anatomy and implications for tendon transfer. *Journal of Hand Surgery*, **17A**, 787–798.
[36] Winters, J. M. and Stark, L. (1988). Estimated mechanical properties of synergistic muscles involved in movements of a variety of human joints. *Journal of Biomechanics*, **21**, 1027–1041.
[37] Amis, A. A., Dowson, D. and Wright, V. (1979). Muscle strengths and musculoskeletal geometry of the upper limb. *Engineering in Medicine*, **8**, 41–48.
[38] Engin, A. E. and Chen, S. M. (1986). Statistical data base for the biomechanical properties of the human shoulder complex. I. Kinematics of the shoulder complex. *Journal of Biomechanical Engineering*, **108**, 215–225.
[39] Garner, B. A. (1998). A musculoskeletal model of the upper limb based on the medical image dataset of the Visible Human Male. *Ph.D. Dissertation*, Department of Mechanical Engineering, University of Texas at Austin, Austin, Texas.
[40] Bassett, R. W., Browne, A. O., Morrey, B. F. and An, K. N. (1990). Glenohumeral muscle force and moment mechanics in a position of shoulder instability. *Journal of Biomechanics*, **23**, 405–415.
[41] An, K. N., Hui, F. C., Morrey, B. F., Linscheid, R. L. and Chao, E. Y. (1981). Muscles across the elbow joint: A biomechanical analysis. *Journal of Biomechanics*, **13**, 765–775.
[42] Cutts, A., Alexander, R. M. and Ker, R. F. (1991). Ratios of cross-sectional areas of muscles and their tendons in a healthy human forearm. *Journal of Anatomy*, **176**, 133–137.
[43] Brand, P. W., Beach, R. B. and Thompson, D. E. (1981). Relative tension and potential excursion of muscles in the forearm and hand. *Journal of Hand Surgery*, **6**, 209–219.
[44] Liu, J., Hughes, R. E., Smutz, W. P., Niebur, G. and An, K. N. (1997). Roles of deltoid and rotator cuff muscles in shoulder elevation. *Clinical Biomechanics*, **2**, 32–38.
[45] Otis, J. C., Jiang, C. C., Wickewicz, T. L., Peterson, M. G., Warren, R. F. and Santner, T. J. (1994). Changes in the moment arms of the rotator cuff and deltoid muscles with abduction and rotation. *Journal of Bone and Joint Surgery*, **76-A**, 667–676.
[46] Hughes, R. E., Niebur, G., Liu, J. and An, K. N. (1998). Comparison of two methods for computing abduction moment arms of the rotator cuff. *Journal of Biomechanics*, **31**, 157–160.
[47] Winters, J. M. and Kleweno, D. G. (1993). Effect of initial upper-limb alignment on muscle contributions to isometric strength curves. *Journal of Biomechanics*, **26**, 143–153.
[48] Otis, J. C., Warren, R. F., Backus, S. I., Santner, T. J. and Mabrey, J. D. (1990). Torque production in the shoulder of the normal young adult male. *American Journal of Sports Medicine*, **18**, 119–123.

[49] Delp, S. L., Grierson, A. E. and Buchanan, T. S. (1996). Maximum isometric moments generated by the wrist muscles in flexion–extension and radial–ulnar deviation. *Journal of Biomechanics*, **29**, 1371–1375.
[50] Hutchins, E. L. (1993). The musculoskeletal geometry of the human elbow and wrist: An analysis using torque–angle relationships. *Masters Thesis*, Biomedical Engineering Program, The University of Texas at Austin.
[51] Van der Helm, F. C. T., Veeger, H. E. J., Pronk, G. M., Van der Woude, L. H. V. and Rozendal, R. H. (1992). Geometry parameters for musculoskeletal modelling of the shoulder system. *Journal of Biomechanics*, **25**, 129–144.
[52] Yamaguchi, G. T., Moran, D. W. and Si, J. (1995). A computationally efficient method for solving the redundant problem in biomechanics. *Journal of Biomechanics*, **28**, 999–1005.
[53] Yamaguchi, G. T., Sawa, A. G., Moran, M., Fessler, M. J. and Winters, J. M. (1990). A survey of human musculotendon actuator parameters. In: Winters, J. M. and Woo, S. L. (Eds.), *Multiple Muscle Systems*, Springer-Verlag, pp. 717–773.
[54] Veeger, H. E., Van der Helm, F. C., Van der Woude, L. H., Pronk, G. M. and Rozendal, R. H. (1991). Inertia and muscle contraction parameters for musculoskeletal modeling of the shoulder mechanism. *Journal of Biomechanics*, **24**, 615–629.
[55] Jacobson, M. D., Raab, R., Fazeli, B. M., Abrams, R. A., Botte, M. J. and Lieber, R. L. (1992). Architectural design of the human intrinsic hand muscle. *Journal of Hand Surgery*, **17A**, 804–809.
[56] Veeger, H. E., Yu, B., An, K. N. and Rozendal, R. H. (1997). Parameters for modeling the upper extremity. *Journal of Biomechanics*, **13**, 647–652.
[57] Bogduk, N., Johnson, G. and Spalding, D. (1998). The morphology and biomechanics of latissimus dorsi. *Clinical Biomechanics*, **13**, 377–385.
[58] Kulig, K., Andrews, J. G. and Hay, J. G. (1984). Human strength curves. *Exercise and Sport Sciences Reviews*, **12**, 417–466.
[59] Reiser, R. (1993). Development of geometric and muscle-specific parameter values for musculoskeletal modeling of the shoulder joint. *Masters Thesis*, Dept. of Kinesiology, University of Texas at Austin.
[60] Engin, A. E. and Kaleps, I. (1980). Active muscle torques about long-bone axes of major human joints. *Aviation, Space, and Environmental Medicine*, **51**, 551–555.
[61] Amis, A. A., Dowson, D. and Wright, V. (1980b). Analysis of elbow forces due to high-speed forearm movements. *Journal of Biomechanics*, **13**, 825–831.
[62] Knapik, J., Wright, J. E., Mawdsley, R. H. and Braun, J. (1983). Isometric, isotonic, and isokinetic torque variations in four muscle groups through a range of joint motion. *Physical Therapy*, **63**, 938–947.
[63] Gonzalez, R. V. (1994). A computational musculoskeletal model of the human elbow and forearm in the analysis of ballistic movements. *Ph.D. Thesis*, Dept. of Mechanical Engineering, The University of Texas at Austin.

APPENDIX

Table IV defines the Obstacle-set parameters used to model the path of each muscle bundle included in the upper-limb model. Each muscle path is modeled with its own unique obstacle set, which

TABLE IV

Muscle	Obstacle		Frame	*X*	*Y*	*Z*	Diameter
subclavius	origin		GROUND	55.88	−20.58	5.90	
(SBCL)	insert		clavicle	87.90	−10.29	6.62	
serratus	origin		GROUND	85.98	−56.61	13.20	
anterior	single	center	GROUND	45.37	−84.90	18.00	−78.88
(superior)		*x*-axis		0.662023	0.134578	0.737302	
(SRAs)		*y*-axis		0.041050	0.975759	−0.214962	
		z-axis		−0.748358	0.172576	0.640451	
	insert		scapula	−110.98	7.34	7.25	
serratus	origin		GROUND	114.81	−12.79	−73.27	
anterior	single	center	GROUND	50.19	−71.35	−58.49	−155.82
(middle)		*x*-axis		0.978158	−0.003986	0.207826	
(SRAm)		*y*-axis		0.043272	0.981817	−0.184832	
		z-axis		−0.203310	0.189788	0.960544	
	insert		scapula	−136.78	4.72	−70.35	
serratus	origin		GROUND	133.24	12.17	−188.49	
anterior	single	center	GROUND	31.14	−60.19	−135.35	−223.16
(inferior)		*x*-axis		0.956825	−0.279102	0.081165	
(SRAi)		*y*-axis		0.283423	0.957817	−0.047525	
		z-axis		−0.064477	0.068477	0.995567	
	insert		scapula	−143.28	14.71	−124.97	

TABLE IV (Continued)

Muscle	Obstacle		Frame	X	Y	Z	Diameter
trapezius	origin		GROUND	1.71	−85.24	142.73	
(C1−C6)	single	center	GROUND	39.22	−69.97	90.34	44.10
(TRPc)		x-axis		0.959081	0.141858	0.245031	
		y-axis		−0.166575	0.982514	0.083181	
		z-axis		−0.228946	−0.120593	0.965940	
	insert		scapula	−29.64	24.54	18.46	
trapezius	origin		GROUND	3.95	−110.51	71.90	
(C7)	single	center	GROUND	45.46	−104.53	39.01	94.60
(TRPc7)		x-axis		0.992873	−0.007211	0.118960	
		y-axis		0.100292	0.589782	−0.801310	
		z-axis		−0.064382	0.807530	0.586302	
	insert		scapula	−6.22	−10.76	−1.34	
trapezius	origin		GROUND	0.00	−124.17	52.18	
(T1)	single	center	GROUND	48.43	−115.93	24.74	103.06
(TRPt1)		x-axis		0.999899	0.010970	0.009010	
(TRPt1)		y-axis		0.000289	0.618811	−0.785540	
		z-axis		−0.014193	0.785464	0.618745	
	insert		scapula	−67.61	−25.07	−0.68	
trapezius	origin		GROUND	2.90	−172.47	−109.82	
(T2−T7)	single	center	GROUND	43.89	−106.80	−69.64	145.44
(TRPt)		x-axis		0.999642	0.022615	0.014307	
		y-axis		−0.020819	0.993127	−0.115173	
		z-axis		−0.016813	0.114834	0.993242	
	insert		scapula	−133.35	−5.33	−41.49	
lev. scap.	origin		GROUND	29.63	−42.51	147.51	
(LVS)	insert		scapula	−112.83	3.39	14.26	
rhomboid	origin		GROUND	1.59	−94.39	85.34	
minor	single	center	GROUND	42.13	−66.79	18.74	151.66
(RMN)		x-axis		0.996157	0.042086	−0.076805	
		y-axis		−0.074467	0.868613	−0.489863	
		z-axis		0.046097	0.493700	0.868410	
	insert		scapula	−126.48	−3.22	−7.24	
rhomboid	origin		GROUND	0.52	−125.50	47.97	
major	single	center	GROUND	42.13	−66.79	18.74	151.66
(T1−T2)		x-axis		0.996157	0.042086	−0.076805	
(RMJt2)		y-axis		−0.074467	0.868613	−0.489863	
		z-axis		0.046097	0.493700	0.868410	
	insert		scapula	−133.87	−2.17	−43.24	
rhomboid	origin		GROUND	2.49	−149.15	−7.75	
major	single	center	GROUND	52.13	−92.46	−51.99	151.18
(T3−T4)		x-axis		0.995761	0.014501	0.090823	
(RMJt3)		y-axis		0.013066	0.955174	−0.295758	
		z-axis		−0.091041	0.295691	0.950936	
	insert		scapula	−144.60	6.25	−97.84	
pec. minor	origin		GROUND	108.26	−7.64	−79.22	
PMN	insert		scapula	−23.86	37.61	−13.41	
pectoralis	origin		clavicle	41.19	5.78	13.69	
major	single	center	GROUND	120.45	−75.20	−19.05	−140.00
(clavicular)		x-axis		0.701715	−0.549153	−0.453903	
(PMJc)		y-axis		0.686887	0.690614	0.226361	
		z-axis		0.189165	−0.470621	0.861819	
	insert		humerus	11.03	17.38	−108.70	

TABLE IV (Continued)

Muscle	Obstacle		Frame	X	Y	Z	Diameter
pectoralis	origin		GROUND	28.03	21.92	−60.15	
major	single	center	GROUND	64.49	−87.37	−73.24	−209.00
(sternal)		x-axis		0.994373	−0.092383	0.051844	
(PMJs)		y-axis		0.099817	0.980988	−0.166429	
		z-axis		−0.035483	0.170667	0.984690	
	insert		humerus	11.27	16.44	−70.82	
pectoralis	origin		GROUND	34.45	50.91	−158.58	
major	single	center	GROUND	46.28	−71.85	−65.73	−202.86
(ribs)		x-axis		0.963313	−0.168136	0.209186	
(PMJr)		y-axis		0.173093	0.984890	−0.005483	
		z-axis		−0.205103	0.041490	0.977860	
	insert		humerus	13.68	16.85	−34.16	
latissimus	origin		GROUND	1.54	−165.15	−187.07	
dorsi	double	center	GROUND	56.67	−99.28	−152.06	148.88
(thoracic)		x-axis		0.182131	−0.982399	0.041482	
(LTDt)		y-axis		0.909848	0.184377	0.371728	
		z-axis		−0.372833	−0.029961	0.927415	
		center	scapula	−23.17	4.57	−53.16	−41.82
		x-axis		0.587568	−0.598997	−0.544028	
		y-axis		0.318034	0.789169	−0.525420	
		z-axis		0.744055	0.135700	0.654193	
	insert		humerus	0.66	15.08	−72.47	
latissimus	origin		GROUND	4.62	−143.55	−360.53	
dorsi	double	center	GROUND	56.13	−95.03	−224.48	164.08
(lumbar)		x-axis		0.954223	−0.278497	−0.109078	
(LTDl)		y-axis		0.294216	0.939619	0.174797	
		z-axis		0.053811	−0.198888	0.978544	
		center	humerus	−5.50	2.99	−57.92	−25.94
		x-axis		0.965787	−0.177168	0.189388	
		y-axis		0.172600	0.984160	0.040480	
		z-axis		−0.193560	−0.006407	0.981068	
	insert		humerus	2.89	14.35	−53.68	
latissimus	origin		GROUND	49.55	−128.04	−419.76	
dorsi	double	center	GROUND	95.01	−73.81	−313.52	117.76
(illiac)		x-axis		0.974275	−0.222249	−0.037328	
(LTDi)		y-axis		0.225351	0.959100	0.171302	
		z-axis		−0.002270	−0.175307	0.984511	
		center	humerus	−5.50	2.99	−57.92	−25.94
		x-axis		0.965787	−0.177168	0.189388	
		y-axis		0.172600	0.984160	0.040480	
		z-axis		−0.193560	−0.006407	0.981068	
	insert		humerus	1.22	16.30	−31.98	
deltoid	origin		clavicle	113.10	−8.75	8.84	
(clavicular)	stub	center	scapula	−30.04	36.63	−45.72	94.30
(DLTc)		x-axis		0.780317	0.571773	0.253336	
		y-axis		0.267389	0.061163	−0.961646	
		z-axis		−0.565338	0.818128	−0.105160	
	via		humerus	16.42	19.96	−81.46	
	insert		humerus	14.97	11.75	−97.71	

TABLE IV (Continued)

Muscle	Obstacle		Frame	*X*	*Y*	*Z*	Diameter
deltoid	origin		scapula	15.76	−17.73	−15.79	
(acromial)	*via*		scapula	15.74	−17.69	−15.78	
(DLTa)	stub	center	scapula	−9.81	9.80	−49.19	92.56
		x-axis		0.796556	−0.603459	−0.036535	
		y-axis		−0.043136	0.003548	−0.999063	
		z-axis		0.603023	0.797386	−0.023206	
	via		humerus	25.81	1.73	−101.03	
	insert		humerus	17.10	10.28	−127.97	
deltoid	origin		scapula	−50.49	−28.96	−9.95	
(scapular)	*via*		scapula	−40.57	−56.12	−31.91	
(DLTs)	stub	center	scapula	−28.92	17.87	−54.89	−142.88
		x-axis		−0.006772	−0.979383	−0.201897	
		y-axis		−0.886566	−0.087512	0.454249	
		z-axis		−0.462552	0.182071	−0.867696	
	via		humerus	17.51	−20.18	−81.73	
	insert		humerus	15.28	0.73	−94.63	
supra-	origin		scapula	−83.09	1.76	0.30	
spinatus	*via*		scapula	−25.68	−2.72	−7.76	
(SUPR)	*via*		humerus	14.88	−5.22	23.31	
	insert		humerus	21.61	−4.10	13.41	
infra-	origin		scapula	−100.71	−8.30	−59.28	
spinatus	*via*		scapula	−32.43	−25.78	−49.62	
(INFR)	stub	center	humerus	−2.72	0.90	4.71	51.06
		x-axis		−0.673837	−0.688533	0.268078	
		y-axis		0.732673	−0.669577	0.121891	
		z-axis		0.095573	0.278548	0.955655	
	insert		humerus	21.78	−8.16	4.29	
sub-	origin		scapula	−99.79	2.78	−63.96	
scapularis	*via*		scapula	−54.22	22.11	−46.80	
(SBSC)	single	center	scapula	−36.26	11.20	−18.87	30.82
		x-axis		0.444473	0.895644	−0.016269	
		y-axis		0.895076	−0.444771	−0.031886	
		z-axis		−0.035795	−0.000388	−0.999360	
	insert		humerus	−6.27	23.51	5.65	
teres	origin		scapula	−69.72	−9.91	−80.07	
minor	*via*		scapula	−53.89	−23.28	−69.87	
(TMN)	stub	center	humerus	2.99	−0.21	3.61	45.86
		x-axis		−0.740369	−0.659446	−0.130323	
		y-axis		0.665751	−0.692562	−0.2777728	
		z-axis		0.092890	−0.292384	0.951779	
	insert		humerus	18.41	−5.89	−23.58	
teres	origin		scapula	−122.43	−3.47	−115.58	
major	single	center	scapula	−96.99	11.55	−111.12	48.00
(TMJ)		*x*-axis		−0.618541	−0.713579	0.328956	
		y-axis		0.529573	−0.687868	−0.496376	
		z-axis		0.580481	−0.132823	0.803368	
	insert		humerus	−7.23	6.36	−46.41	
coraco-	origin		scapula	−12.26	37.00	−24.64	
brachialis	single	center	scapula	−46.16	4.34	−63.32	34.62
(CRCB)		*x*-axis		0.183782	0.668114	−0.721005	
		y-axis		0.424200	−0.715588	−0.554967	
		z-axis		−0.886723	−0.203856	−0.414926	
	via		humerus	−8.34	19.82	−96.84	
	insert		humerus	−2.61	9.81	−160.82	

TABLE IV (Continued)

Muscle	Obstacle		Frame	*X*	*Y*	*Z*	Diameter
triceps	origin		scapula	−36.99	−5.16	−64.53	
brachii	double	center	humerus	35.69	81.15	−125.51	244.38
(long)		*x*-axis		0.108539	0.966166	0.233973	
(TRCIg)		*y*-axis		−0.514207	−0.146864	0.844998	
		z-axis		0.850770	−0.212026	0.480869	
		center	humerus	3.70	26.26	−290.64	58.00
		x-axis		−0.101600	−0.654426	0.749269	
		y-axis		−0.029157	−0.750884	−0.659790	
		z-axis		0.994398	−0.088881	0.057209	
	insert		ulna	0.05	−24.89	9.99	
triceps	origin		humerus	−7.30	−1.08	−169.44	
brachii	*via*		humerus	−23.82	13.16	−218.29	
(medial)	single	center	humerus	16.19	19.10	−298.10	50.08
(TRCm)		*x*-axis		−0.185601	−0.498201	0.846964	
		y-axis		−0.325493	−0.782107	−0.531378	
		z-axis		0.927150	−0.374305	−0.017001	
	insert		ulna	0.05	−24.89	9.99	
triceps	origin		humerus	1.15	−6.73	−87.07	
brachii	*via*		humerus	13.88	−25.46	−149.46	
(lateral)	single	center	humerus	4.35	20.64	−294.10	45.58
(TRCIt)		*x*-axis		0.013100	−0.647492	0.761960	
		y-axis		0.086586	−0.758428	−0.645979	
		z-axis		0.996158	0.074437	0.046128	
	via		ulna	8.63	−25.04	5.84	
	insert		ulna	0.05	−24.89	9.99	
biceps	origin		scapula	−8.13	29.22	−21.49	
brachii	double	center	scapula	−13.10	9.06	−45.19	48.54
(short)		*x*-axis		−0.499926	−0.531809	0.683560	
(BICs)		*y*-axis		0.466605	0.499534	0.729893	
		z-axis		−0.729625	0.683845	−0.001586	
		center	humerus	15.05	−7.51	−277.12	102.90
		x-axis		0.511716	−0.083701	0.855068	
		y-axis		−0.106939	0.981298	0.160055	
		z-axis		−0.852474	−0.173343	0.493195	
	insert		radius	−3.61	12.99	−48.88	
biceps	origin		scapula	−15.09	8.30	−24.60	
brachii	sphere	center	humerus	0.00	0.00	0.00	50.50
(long)	*via*		humerus	10.20	22.36	1.15	
(BICI)	single	center	humerus	15.05	−7.51	−277.12	102.90
		x-axis		0.511716	−0.083701	0.855068	
		y-axis		−0.106939	0.981298	0.160055	
		z-axis		−0.852474	−0.173343	0.493195	
	insert		radius	−3.61	12.99	−48.88	
brachialis	origin		humerus	6.36	17.03	−215.43	
(BRA)	*via*		humerus	9.99	30.16	−238.35	
	single	center	humerus	62.17	12.24	−287.47	70.46
		x-axis		0.009991	0.257742	0.966162	
		y-axis		−0.035667	0.965687	−0.257247	
		z-axis		−0.999314	−0.031890	0.018841	
	insert		ulna	2.52	−3.67	−31.57	

TABLE IV (Continued)

Muscle	Obstacle		Frame	X	Y	Z	Diameter
brachio-	origin		humerus	14.67	4.13	−219.42	
radialis	*via*		humerus	22.80	8.70	−229.69	
(BRD)	double	center	humerus	3.60	8.98	−295.60	−64.56
		x-axis		−0.019232	−0.644344	0.764494	
		y-axis		0.285131	−0.736417	−0.613507	
		z-axis		0.958296	0.206182	0.197885	
		center	radius	−4.46	−4.54	−153.15	14.34
		x-axis		0.057794	−0.996958	0.052280	
		y-axis		0.997196	0.055157	−0.050572	
		z-axis		0.047534	0.055057	0.997351	
	via		radius	1.42	−5.08	−190.29	
	insert		radius	2.49	0.37	−261.23	
supinator	origin		ulna	21.02	−20.40	−48.40	
(SUP)	single	center	radius	−11.10	−5.70	−98.50	25.72
		x-axis		0.944097	0.327940	−0.033699	
		y-axis		−0.328977	0.943796	−0.031978	
		z-axis		0.021318	0.041277	0.998920	
	via		radius	11.02	−3.68	−85.21	
	insert		radius	−1.02	3.76	−92.22	
pronator	origin		humerus	−14.01	12.53	−281.76	
teres	*via*		humerus	−20.92	26.66	−289.58	
(PRNT)	single	center	humerus	6.83	26.15	−305.64	35.16
		x-axis		−0.337350	0.298173	0.892910	
		y-axis		−0.445202	0.785204	−0.430407	
		z-axis		−0.829452	−0.542723	−0.132141	
	insert		radius	2.13	1.59	−120.51	
flexor	origin		humerus	−22.36	21.46	−300.67	
carpi	*via*		radius	1.07	10.09	−224.06	
radialis	single	center	hand	12.94	6.05	5.16	23.58
(FCR)		*x*-axis		0.128442	−0.025899	0.991379	
		y-axis		−0.026955	0.999198	0.029596	
		z-axis		−0.991350	−0.030524	0.127640	
	via		hand	11.89	11.19	−7.13	
	insert		hand	13.56	9.11	−20.64	
flexor	origin		humerus	−14.90	14.18	−306.38	
carpi	*via*		ulna	−21.48	−24.51	−161.59	
ulnaris	single	center	hand	0.46	7.68	4.90	24.90
(FCU)		*x*-axis		0.032300	0.002555	0.999475	
		y-axis		−0.012684	0.999917	−0.002146	
		z-axis		−0.999397	−0.012608	0.032329	
	insert		hand	−16.91	14.21	−6.42	
extensor	origin		humerus	19.68	8.07	−259.80	
carpi	*via*		humerus	28.90	22.07	−273.31	
radialis	single	center	humerus	10.35	26.88	−303.23	29.66
longus		*x*-axis		−0.185839	−0.834077	0.519403	
(ECRL)		*y*-axis		0.034932	0.522669	0.851820	
		z-axis		−0.981959	0.176445	−0.067996	
	via		radius	10.50	−9.57	−149.61	
	via		radius	−3.10	−9.46	−271.53	
	single	center	carpal	0.71	4.07	−6.61	30.80
		x-axis		−0.119154	0.002427	0.992873	
		y-axis		−0.004987	−0.999985	0.001845	
		z-axis		0.992863	−0.004732	0.119165	
	via		hand	14.42	−9.56	−17.20	
	insert		hand	16.17	−6.45	−32.67	

TABLE IV (Continued)

Muscle	Obstacle		Frame	X	Y	Z	Diameter
extensor	origin		humerus	30.36	17.02	−286.52	
carpi	single	center	humerus	24.61	−7.75	−303.06	46.18
radialis		x-axis		0.033604	0.020741	0.999220	
brevis		y-axis		0.870739	0.490160	−0.039457	
(ECRB)		z-axis		−0.490596	0.871386	−0.001589	
	via		radius	−5.50	−14.27	−274.95	
	single	center	carpal	0.71	4.07	−6.61	30.80
		x-axis		−0.119154	0.002427	0.992873	
		y-axis		−0.004987	−0.999985	0.001845	
		z-axis		0.992863	−0.004732	0.119165	
	via		hand	12.36	−9.63	−20.49	
	insert		hand	12.11	−7.13	−31.66	
extensor	origin		humerus	33.37	20.66	−302.57	
carpi	*via*		humerus	35.69	20.81	−309.12	
ulnaris	*via*		ulna	22.31	−22.64	−109.34	
(ECU)	*via*		ulna	3.49	−5.08	−261.28	
	single	center	radius	−3.13	−6.01	−270.73	20.00
		x-axis		0.075061	0.011266	0.997115	
		y-axis		−0.339016	−0.940086	0.036142	
		z-axis		0.937781	−0.340751	−0.066745	
	via		hand	−24.74	−3.65	−7.39	
	insert		hand	−24.61	−0.48	−17.86	

may consist of an origin site, any number of fixed *via* points, any number of obstacles, and an insertion site. Under the Obstacle column, the components comprising an obstacle set are listed in the order in which they appear in the muscle path. For example, the obstacle set modeling the acromial (middle) head of deltoid consists of an origin site, a single fixed *via* point, a sphere-capped cylinder obstacle (stub), another fixed *via* point, and an insertion site, in that order. For each origin site, *via* point, and insertion site, the Frame column specifies the body to which the point in question is attached; and the X, Y, and Z columns specify the coordinates of the point, expressed in the reference frame of that body. For example, the first *via* point in the acromial deltoid path is fixed in the scapula frame at coordinates (15.74, −17.69, −15.78). In general, four types of obstacles can be used to model muscle paths [33]: a single sphere (sphere), a single cylinder (single), a double cylinder (double), and a sphere-capped cylinder (stub). The description of each obstacle occupies four lines in the table (eight lines for the double cylinder). The first line locates the center of the obstacle. Within this line, the Frame column specifies the body to which the center of the obstacle is attached; the X, Y, and Z columns specify the coordinates of the center of the obstacle, expressed in the reference frame of that body; and the Diameter column specifies the diameter of the obstacle. The next three lines define the orientation of each orthogonal axis in the obstacle's reference frame. For example, the y-axis of the sphere-capped cylinder in the acromial deltoid path is fixed in the scapula frame with x-, y-, and z-components of −0.043136, 0.003548, and −0.999063, respectively. For a double-cylinder obstacle, four additional lines are given in the table to describe the position and orientation of the second cylinder.

COLOUR PLATE I (see page 96, figure 1) Computer-generated rendering of the bone and muscle surfaces reconstructed from the VHM image dataset. The data representing each surface is in the form of a dense mesh of connected triangles. The triangular meshes shown in the figure have been passed through a geometry-preserving decimation algorithm to reduce the mesh density by about 90% (see text). The reconstructed surface data constitute an accurate, high-resolution, anatomical database from which the upper-limb model was developed

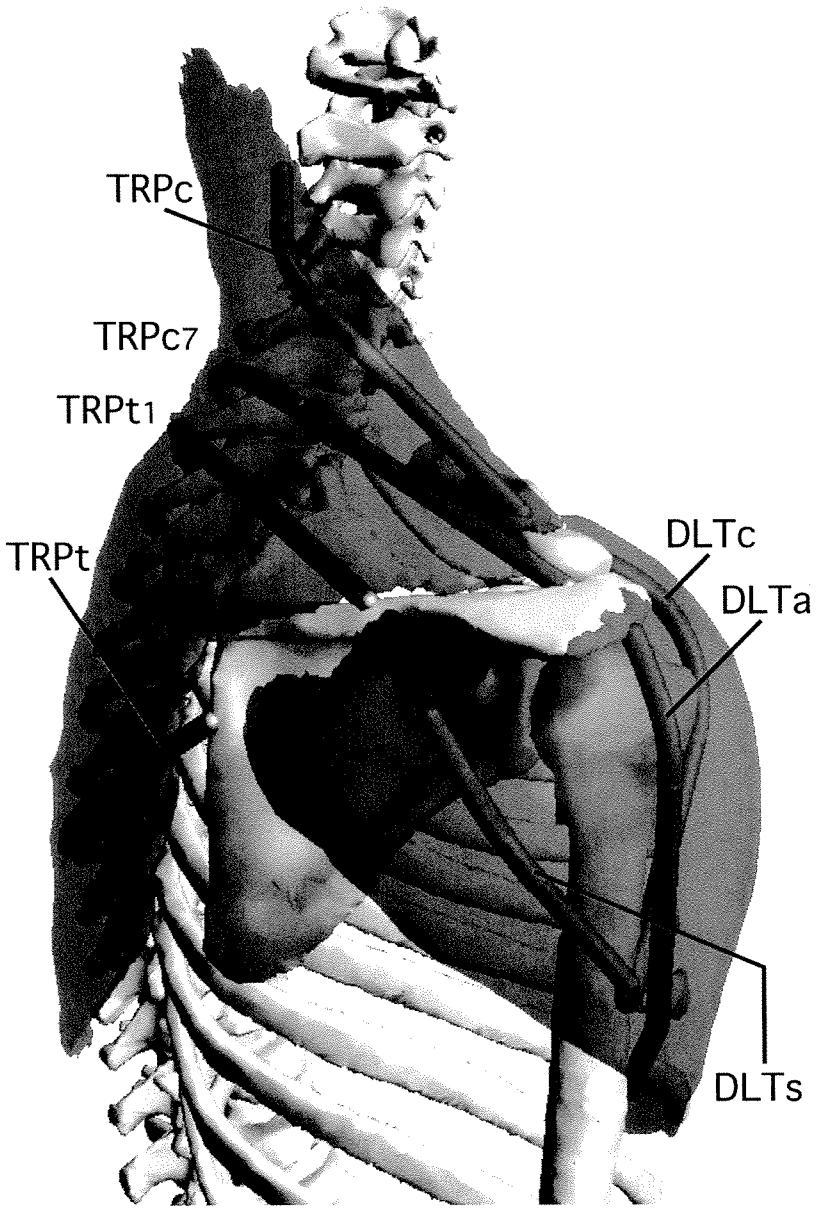

COLOUR PLATE II (see page 97, figure 2) Computer-generated rendering of the fan-shaped trapezius and deltoid muscles. Multiple paths were used to model the action of each muscle group. Trapezius was separated into four bundles and deltoid was separated into three bundles in the model (see text for details). Muscle abbreviations are given in Figure 8 and Table I

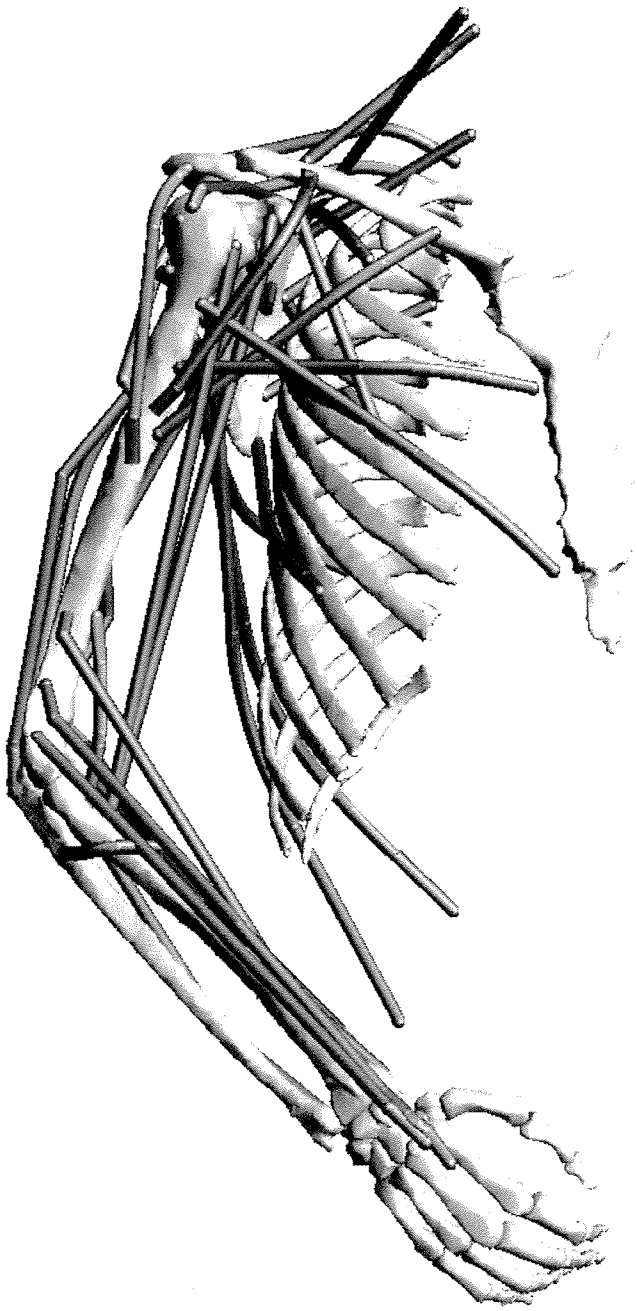

COLOUR PLATE III (see page 98, figure 3) Antero-lateral view of the reconstructed bone surfaces overlaid with the modeled muscle paths. Forty-two muscle bundles were used to represent the actions of 26 muscle groups in the upper limb. Muscle abbreviations are given in Figure 8 and Table I

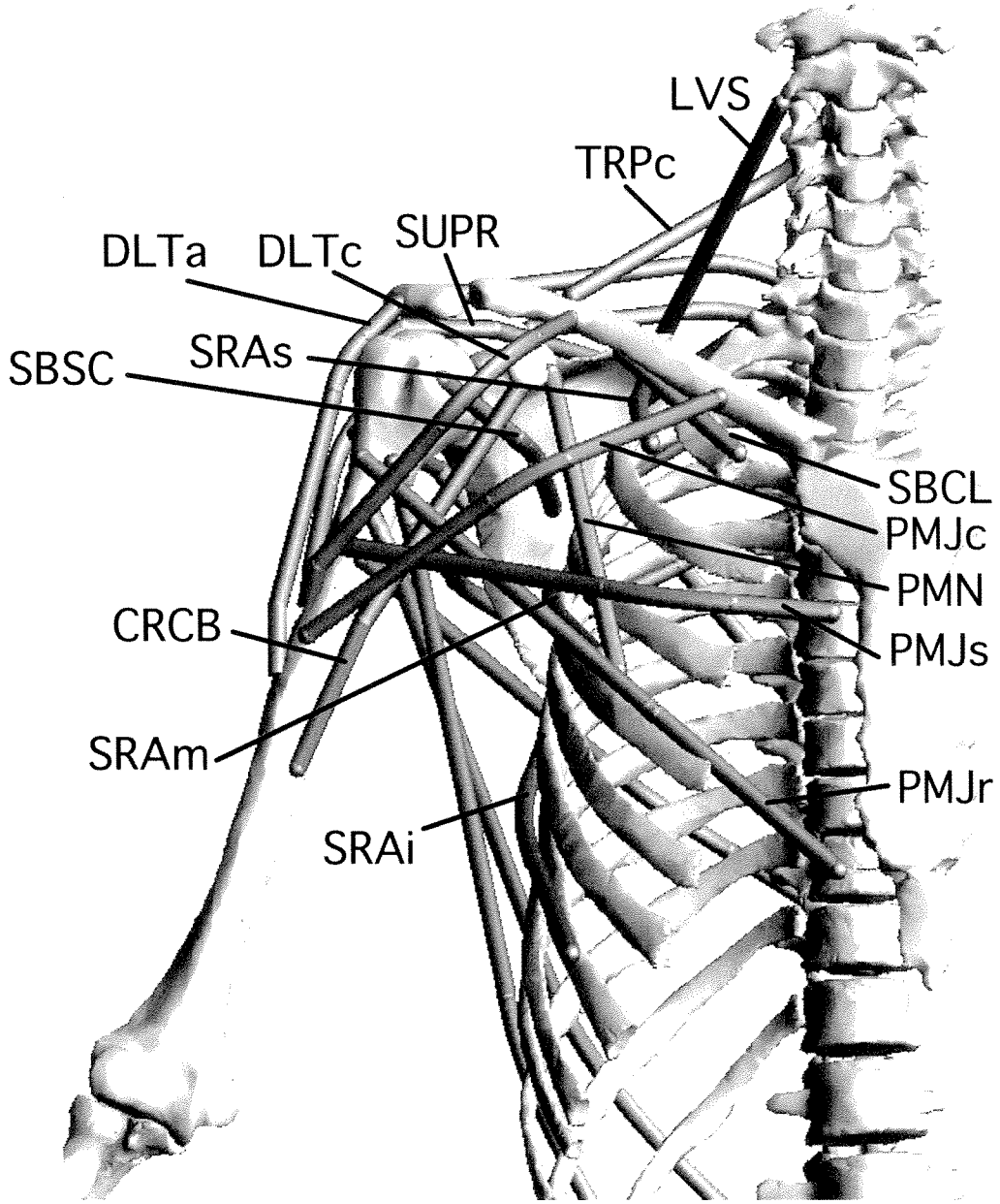

COLOUR PLATE IV (see page 99, figure 4) Anterior view showing the modeled muscle paths crossing the shoulder. See Figure 8 and Table I for muscle abbreviations

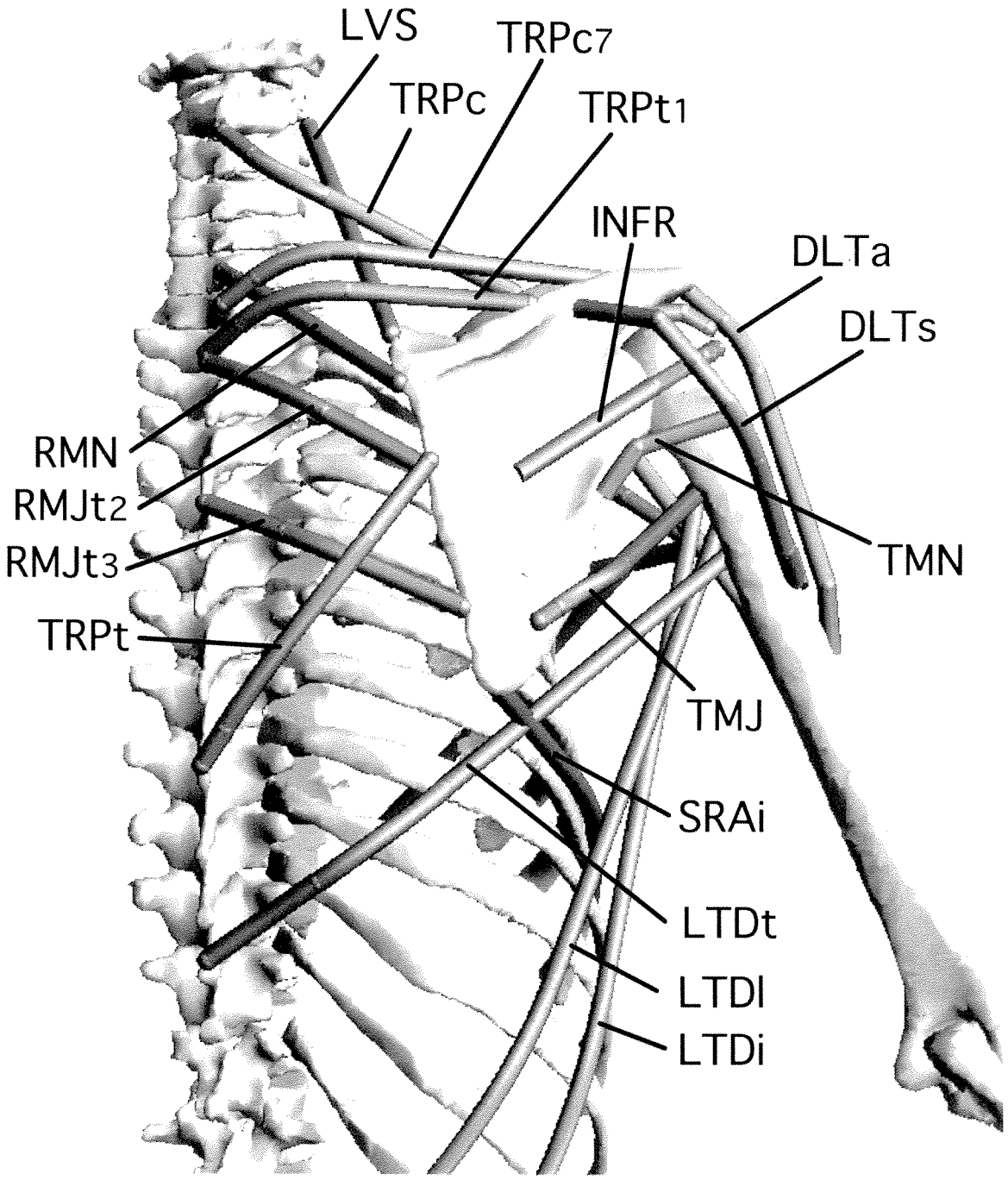

COLOUR PLATE V (see page 100, figure 5) Posterior view showing the modeled muscle paths crossing the shoulder. See Figure 8 and Table I for muscle abbreviations

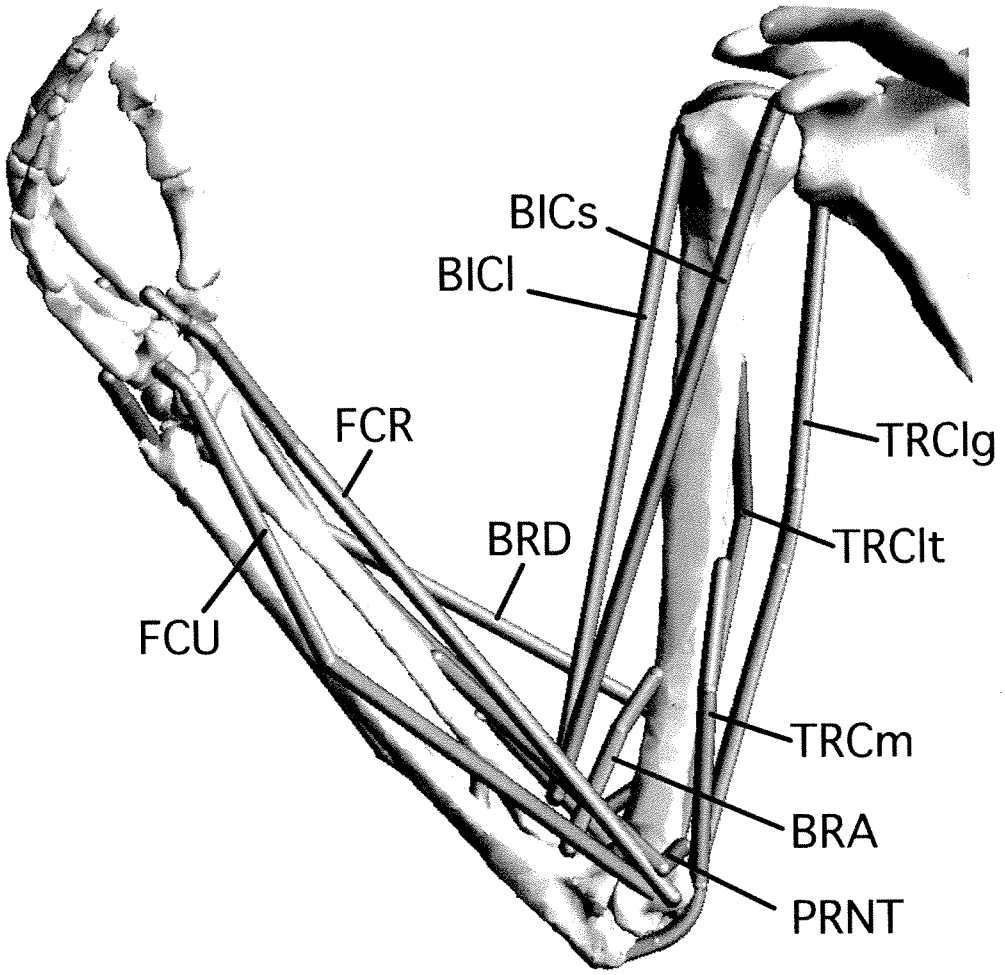

COLOUR PLATE VI (see page 101, figure 6) Anterior view of the modeled muscle paths crossing the elbow and wrist. Muscle abbreviations are given in Figure 8 and Table I

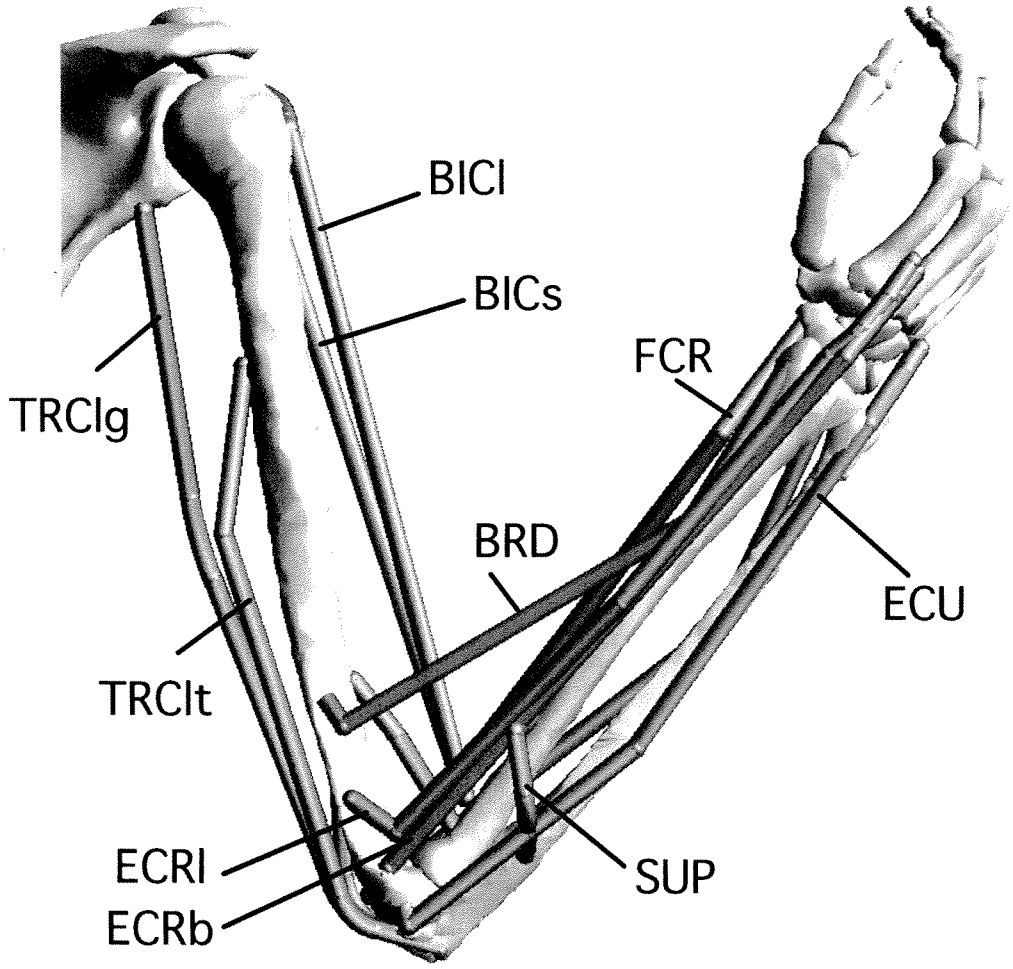

COLOUR PLATE VII (see page 102, figure 7) Posterior view of the modeled muscle paths crossing the elbow and wrist. See Figure 8 and Table I for muscle abbreviations